

# Open Research Online

---

The Open University's repository of research publications and other research outputs

## Mush remobilisation and mafic recharge: A study of the crystal cargo of the 2013–17 eruption at Volcán de Colima, Mexico

### Journal Item

#### How to cite:

Hughes, Gerallt E.; Petrone, Chiara Maria; Downes, Hilary; Varley, Nick R. and Hammond, Samantha J. (2021). Mush remobilisation and mafic recharge: A study of the crystal cargo of the 2013–17 eruption at Volcán de Colima, Mexico. *Journal of Volcanology and Geothermal Research*, article no. 107296.

For guidance on citations see [FAQs](#).

© 2021 Elsevier Ltd.



<https://creativecommons.org/licenses/by-nc-nd/4.0/>

Version: Accepted Manuscript

Link(s) to article on publisher's website:

<http://dx.doi.org/doi:10.1016/j.jvolgeores.2021.107296>

---

Copyright and Moral Rights for the articles on this site are retained by the individual authors and/or other copyright owners. For more information on Open Research Online's data [policy](#) on reuse of materials please consult the policies page.

---

## Journal Pre-proof

Mush remobilisation and mafic recharge: A study of the crystal cargo of the 2013–17 eruption at Volcán de Colima, Mexico

Gerallt E. Hughes, Chiara Maria Petrone, Hilary Downes, Nick R. Varley, Samantha J. Hammond



PII: S0377-0273(21)00125-6

DOI: <https://doi.org/10.1016/j.jvolgeores.2021.107296>

Reference: VOLGEO 107296

To appear in: *Journal of Volcanology and Geothermal Research*

Received date: 19 February 2021

Revised date: 18 May 2021

Accepted date: 21 May 2021

Please cite this article as: G.E. Hughes, C.M. Petrone, H. Downes, et al., Mush remobilisation and mafic recharge: A study of the crystal cargo of the 2013–17 eruption at Volcán de Colima, Mexico, *Journal of Volcanology and Geothermal Research* (2021), <https://doi.org/10.1016/j.jvolgeores.2021.107296>

This is a PDF file of an article that has undergone enhancements after acceptance, such as the addition of a cover page and metadata, and formatting for readability, but it is not yet the definitive version of record. This version will undergo additional copyediting, typesetting and review before it is published in its final form, but we are providing this version to give early visibility of the article. Please note that, during the production process, errors may be discovered which could affect the content, and all legal disclaimers that apply to the journal pertain.

© 2021 Published by Elsevier B.V.

## Mush remobilisation and mafic recharge: A study of the crystal cargo of the 2013-17 eruption at Volcán de Colima, Mexico

Hughes, Gerallt E.<sup>1,2\*</sup>; Petrone, Chiara Maria<sup>1</sup>; Downes, Hilary<sup>2</sup>; Varley, Nick R.<sup>3</sup>, Hammond, Samantha J.<sup>4</sup>

<sup>1</sup> Department of Earth Sciences, Natural History Museum, Cromwell Road, London SW5 7BD, UK.

<sup>2</sup> Department of Earth and Planetary Sciences, Birkbeck, University of London, Malet Street, London WC1E 7HX, UK.

<sup>3</sup> Colima Intercambio e Investigación en Vulcanología (CIIV), Facultad de Ciencias, Universidad de Colima, Calle Bernal Díaz del Castillo 340, Villas San Sebastián, 28045 Colima, Colima, Mexico.

<sup>4</sup> School of Environment, Earth and Ecosystem Sciences, Open University, Walton Hall, Milton Keynes MK7 6AA, UK.

\*Corresponding author, email address: g.hughes@nhm.ac.uk

Manuscript Type: Research Paper

### ABSTRACT

Volcán de Colima is a highly active stratovolcano at the western end of the Trans-Mexican Volcanic Belt. Present-day activity consists of lava dome growth and destruction, lava flows, small explosions, and larger explosive Vulcanian eruptions; and it has been postulated that increased frequency of more mafic eruptions signals the run-up of c. 100-year eruptive 'cycles', terminating with a Plinian eruption such as those in 1818 and 1913. It is therefore important to understand the role played by mafic recharge during interplinian activity. We present new petrological and geochemical data for lava and ash from the 2013-17 phase of eruption. The uniform paragenesis and geochemical homogeneity of bulk rocks indicate efficient long-term homogenisation of magmas within the plumbing system, similar to the previous 1998-2005 eruptive products. Mineral chemistry however preserves complex patterns of magma recharge and mixing. Chemical and textural information support the interpretation of two magmatic end-members – an evolved end-member saturated with respect to Fe-Ti oxides and apatite and crystallising low-An plagioclase and pyroxenes in the Mg# 69-75 range; and a more primitive, mafic end-member crystallising high-An plagioclase and pyroxenes in the Mg# 77-88 range. Pyroxene textures and zoning patterns suggest mixing of the mafic melts with the evolved magma and remobilisation of the crystal mush. Two-pyroxene geothermometry constrains magmatic temperatures to c. 980-1000°C for the evolved end-member, and c. 1020-1080°C for the mafic end-member. Pressure estimates suggest crystallisation at 4-6 kbar, or c. 12-18 km depth. We interpret this to reflect periodic injections of mafic melts and remobilised crystals into

evolved reservoirs in a mushy magma storage system in the mid-crust, in agreement with geophysical data suggesting a semi-molten, partially crystallised body at this depth. From 2015, an increase in reverse zoned crystals, indicative of mafic injection, suggests that these melts were injected into the system following the large eruption in July 2015. Our findings suggest that the intense July 2015 eruption may be linked to increased input of mafic magmas into the shallow system, indicating that mafic injections may be a key process governing the timing and style of eruption at Volcán de Colima.

Keywords: Volcán de Colima, magma mixing, crystal mush, mafic recharge, volcanic plumbing systems, crystal cargo

## 1. INTRODUCTION

Magma recharge and mixing in volcanic arc systems are processes which modulate the composition of erupted products and their constituent minerals (e.g. Streck, 2008). Mafic recharge into evolved magma reservoirs provides additional heat and volatiles that can trigger eruptions on a variety of scales (e.g., Anderson, 1976; Sparks et al., 1977; Fichtlberger et al., 2006; Murphy et al., 2000; Cashman and Giordano, 2014; Ruprecht and Frank, 2013; Ruprecht and Bachmann, 2010). However, efficient mixing processes can homogenise the bulk chemistry of magmas (Mangler et al., 2019) obscuring the occurrence of such a process, which is instead preserved in the crystal cargo. Therefore, textural and compositional information contained in the crystal cargo is used to unlock important information about magma mixing and the state of the magmas (e.g., Putirka, 2008; Blundy and Cashman, 2008) that cannot otherwise be accessed (Holness et al., 2019; Bachmann and Huber, 2016; Cashman et al., 2017; Mangler et al., 2020).

Volcán de Colima is a highly active stratovolcano in western Mexico. It presents a significant hazard to over half a million people (Gavilanes-Ruiz et al., 2009). Like other volcanoes in the Trans-Mexican Volcanic Belt (TMVB; e.g. Popocatepetl, Martin-Del Pozzo et al., 2016; Citlaltépetl-Pico de Orizaba, Schaaf and Carrasco-Núñez, 2010; Ceboruco, Sieron and Siebe, 2008), Volcán de Colima exhibits a variety of styles of activity, from explosive sub-Plinian to Plinian eruptions to less-intense effusive and explosive periods. It has been suggested that these Plinian events are experienced on average every century (Luhr and Carmichael, 1980, 1990; Robin et al., 1991; Breton-González et al., 2002), interspersed by periods of effusive lava flows and dome growth with small-to-medium sized Vulcanian explosive eruptions. The most recent Plinian events at Volcán de Colima occurred in 1818 and 1913 (Saucedo et al., 2005). This proposed cyclicity, and the frequent and sometimes intense interplinian activity, make it critical to study the most recent volcanic deposits for insights into the

current state of the magmatic system and to assess the potential for a transition to a more explosive phase.

Whilst the precise role of magma recharge and mixing during Plinian eruptions at Volcán de Colima is still subject to debate (Atlas et al., 2006; Crummy et al., 2014; Macías et al., 2017; Saucedo et al., 2010; Savov et al., 2008; Luhr et al., 2010), most authors agree that injection of mafic melts originate from deeper parts of the volcanic system itself (e.g. Atlas et al., 2006; Macías et al., 2017), or as some have argued, the occasional input of alkalic magmas related to nearby alkali basalt cinder cones (Crummy et al., 2014; Luhr et al., 2010), can provide a trigger for the Plinian eruptions. However, the role of magma recharge during the interplinian phases has been given comparatively little attention, despite its importance for forecasting future catastrophic eruptions. For example, Mangler et al. (2019) using the record of poorly studied interplinian effusive eruptions at Popocatepetl, highlighted the role of recharge following large eruptions and gradual homogenisation, occasional tapping of lower crustal magmas associated with specific eruptions, and flank eruptions that bypass most of the plumbing system altogether. The long-term dynamics of such an active system would otherwise be missed if Plinian eruptions were looked at in isolation (Mangler et al., 2019). Luhr and Carmichael (1980, 1990) suggested that the activity at Volcán de Colima becomes gradually more mafic prior to a Plinian event, implying that magma recharge and mixing occurs during the interplinian phase, and may increase in frequency and volume until a Plinian event is triggered. It is therefore crucial to understand the role of possible mafic injections during the most recent activity.

Here, we present new petrological and geochemical data for both rocks and ash samples from effusive and small explosive eruptions during the highly active 2013-17 eruptive phase. The chemical evolution and magmatic recharge recorded in mineral phases in these samples are discussed, with particular focus on the varied textures and compositions of pyroxene phenocrysts. As pyroxenes grow over a significant range of P-T-X conditions, they will be used to constrain the pre-eruptive magmatic conditions and the nature of the plumbing system. Finally, we interpret these observations in light of existing models and determine the significance of magma mixing events recorded in the interplinian crystal cargoes with respect to the recent activity as well as the potential for future eruptions.

## 2. GEOLOGICAL CONTEXT

Volcán de Colima is a 3860 m high stratovolcano in the western part of the TMVB (Luhr and Carmichael, 1980) (Fig. 1). The TMVB is a 1000 km long, east-west trending continental volcanic arc,

formed by subduction of the Rivera and Cocos plates in a north-east direction beneath the North American plate (Allan and Carmichael, 1984). The TMVB has a complex tectonic and geodynamic history, reflected in its diverse volcanic activity (e.g., Gómez-Tuena et al., 2011; Petrone et al., 2014; Ferrari et al., 2012).

Some of the oldest volcanism at the Colima Volcanic Centre (CVC) include cinder cones, erupted from 12 Ma to 0.06 Ma (Luhr and Carmichael, 1981; Allan and Carmichael, 1984; Carmichael et al., 2006) and scattered to the north of the current edifice; and the oldest mature edifice of the CVC, El Cántaro, is a composite stratovolcano at least 1.7 million years old (Luhr and Carmichael, 1980; Allan, 1986; Luhr and Carmichael, 1990). Volcanism migrated southward to form the Nevado de Colima complex at 0.53 Ma (Luhr and Carmichael, 1980; Robin et al., 1987; Luhr and Presteggaard, 1988; Robin et al., 1990; Cortés et al., 2010). The final stages of activity of Nevado overlapped with the formation of the first edifice close to the current Volcán de Colima, sometimes referred to as Palaeofuego, at approximately 40 ka (Luhr et al., 2010), although some have argued for volcanism at Volcán de Colima at 97 ka or earlier (Cortés et al., 2019). This earlier edifice underwent several collapse events, including an event at c. 7 ka which possibly formed the caldera rim structure to the north of the current edifice known as the Playón (Cortés et al., 2019) (Fig. 1B). Although Cortés et al. (2019) argues that the current edifice grew within the collapse structure, the presence of debris-avalanche deposits, dated at c. 3.6 and 2.5 ka, suggest that the modern edifice has experienced at least partial destruction and collapse, and that the scars from these events are buried beneath later volcanic deposits (Cortés et al., 2019).

#### *Modern Activity*

At least five major eruptions as well as numerous accounts of interplinian activity have been recorded at Volcán de Colima since the mid-1500s (Breton-González et al., 2002). Scientific observations of eruptions were recorded during the 1818 and 1913 Plinian events (Waitz, 1915; Breton-González et al., 2002; Saucedo et al., 2010; Macías et al., 2017) and, since the 1980s, the volcano has been actively studied. Following the 1913 eruption, effusive activity slowly refilled the crater, and significant lava flows and small explosive eruptions occurred in 1961-62, 1975-76, 1981-82 and 1991, followed by periods of intense effusive and explosive activity in 1998-2005, slow dome growth in 2007-2011, and, most recently, intense effusive and explosive activity in 2013-2017. A comprehensive account of the modern activity is given by Varley (2019) and references therein.

The 2013-17 eruptive period was similar in eruptive style to the preceding 1998-2005 activity. Both comprised effusive lava flows and phases of dome-building and destruction via small to moderate

explosive activity and associated ash fall (Arámbula-Mendoza et al., 2018; Varley, 2019; Arámbula-Mendoza et al., 2020). On the basis of eruptive style, and for the purposes of this study, we split the activity into six broad phases, with reference to the simplified timeline in Figure 2:

- *Phase 1 (January 2013-September 2014)* – Following quiescence since mid-2011, activity resumed in January 2013 with Vulcanian explosions which partially destroyed the previous dome, followed by slow dome-growth and periodic Vulcanian explosions, frequently generating small pyroclastic density currents (PDC). This type of activity characterised Phase 1. A short lava flow resulted from magma overtopping the crater early on during this phase.
- *Phase 2 (September 2014-June 2015)* – Increased effusive activity in June 2014 resulted in lava overtopping the crater and the formation of several lava flows to the south-west, west and north-west, and later to the north by June 2015, along with intermittent Vulcanian explosions.
- *Phase 3 (July 2015)* – Due to its high intensity (VEI 3, Newhall and Self, 1982; Reyes-Davila et al., 2016), the 10-11<sup>th</sup> July 2015 event is separated into its own phase. The eruption was complex, with a significant increase in the magma ascent rate resulting in the rapid collapse of lava domes generating multiple pulses of PDCs in two principal episodes over the two days. This was one of the largest and most powerful explosions seen at Volcán de Colima since the 1913 Plinian event, and emplaced a 10 km-long PDC deposit within Montegrande and upper San Antonio ravines on the southern flank of the edifice (Fig. 1; Macorps et al. 2018).
- *Phase 4 (July 2015-December 2015)* – Following the July 2015 eruption, a lava flow quickly descended the southern flank of the cone from July to September 2015 on the upper parts of Montegrande ravine (Fig. 1). Effusion had stopped by late-September 2015 and occasional explosions continued until January 2016.
- *Phase 5 (January 2016-December 2016)* – Effusive activity recommenced in January 2016 with new dome growth and small explosions with ash falls, which persisted through most of the year. This activity culminated in the eruption of a voluminous lava flow on the southern flank of the edifice on top of the earlier 2015 flow, which continued until the end of 2016.
- *Phase 6 (January 2017-March 2017)* - From the end of 2016 to the last explosions in February 2017, a number of powerful explosions resulted in the emplacement of small PDC deposits in the Playón area and La Arena ravine on the north and eastern sides of the edifice respectively. Explosive and effusive activity ceased in Spring 2017.

### 3. METHODS

Twenty-seven rock samples (comprising lava, ballistic ejecta and crystalline pyroclastic material) were collected during fieldwork in April to June 2018, and a further 67 rock samples and 25 ash samples (1 from 2013, 1 from 2014, 10 from 2015, and 11 from 2016) with contextual data were obtained from the collections of Colima Intercambio e Investigación en Vulcanología (CIIV), University of Colima. The crystalline material emplaced within the pyroclastic deposits represent fragments of the recently-erupted dome, based on the observed dome-growth and destruction patterns at Volcán de Colima, and the vesicularity and crystallinity of the samples. Sample preparation was undertaken at the Natural History Museum, London (NHM). Samples for whole-rock analysis were crushed and milled into fine powders. For mineral analysis, polished thin sections were prepared from rock chips of lava and crystalline pyroclastic material; and ash fragments were mounted in 25 mm diameter epoxy resin blocks.

#### *Whole-rock Major Elements*

Whole rock analysis was undertaken on 62 rock and 23 ash samples of sufficient volume (Supplementary Tab. 1). Whole-rock major elements were analysed using X-ray fluorescence (XRF) techniques following the lithium borate flux-fusion technique of Norrish and Hutton (1969) using a Panalytical Axios Advanced wavelength-dispersive XRF analyser by Activation Laboratories Ltd, Ancaster, Canada. Six reference materials (AN-C, BE-N, AC-E, BIR-1a, NCS DC73304 and GBW 07109) were included in the analytical run and prepared in the same preparation method as the natural samples. Duplicates of two samples and a procedural blank sample were also included in the analytical run. The results of the analysis are precise to within 5% for most elements and most detection limits were  $\leq 0.01$  wt %. All whole-rock data has been normalised to 100% on an anhydrous basis.

#### *Whole-rock Trace Elements*

Whole-rock trace elements were analysed using inductively coupled plasma mass spectrometer (ICP-MS) techniques at the Open University, Milton Keynes, UK (Supplementary Tab. 1). The samples were prepared and processed for trace element data in three batches, in December 2018, January 2019 and September 2019 respectively. The samples were prepared using HF-HNO<sub>3</sub> acid digestion and made into 1000-fold dilution solutions for analysis using an Agilent 8800 ICP-QQQ-MS. Five reference materials (BIR-1, W-2, DNC-2, BHVO-2, AGV-1) were used for Batches 1 and 2, plus an additional two reference materials (BCR-2 and RGM-1) were used for Batch 3. Duplicates of the natural samples and a total procedural blank sample were prepared for each batch run and analysed.



For each batch, an additional digest of the USGS reference standard BHVO-2 plus a natural sample was selected at random from the batch to act as a duplicate unknown monitor to assess accuracy and precision. A procedural blank was also processed at the same time as the samples and analysed within the analytical run. Between each 5 samples analysed, the reference material monitor, a natural sample monitor, and a 2% HNO<sub>3</sub> solution monitor was run. The corrected repeat measurements of the reference material BHVO-2 were then used to assess precision and accuracy. Preferred BHVO-2 values from the Open University were used to assess accuracy.

Accuracy is better than 5% relative error (RE) for most samples in all three batches. Exceptions include Cr (9.1 and 7.4% RE for Batches 1 and 2), Ti (6.85% in Batch 3) heavy elements including Yb (5.06-7.04% in all three batches), W, Tl, and Pb; and elements close to or below the detection limit (e.g. Se, Te). A full list is provided in Supplementary Table 1B.

Within-run precision was assessed by the variation in the reference and natural monitor samples assessed as a percentage Relative Standard Deviation (% RSD). Precision is better than 5% RSD for most elements for the BHVO-2 reference standard in all three batches, with the exception of Li, Mg, Yb and W (5.20, 5.56, 5.53, and 11.36% RSD respectively) in Batch 2, and Te in Batches 1 and 2 (11.54 and 13.42% RSD respectively), although this is likely due to low values below or near the detection limit. The procedural blanks were below detection limits for all elements.

Analyses were undertaken in no gas mode, He collisional gas mode and, in some cases, an O<sub>2</sub> reactive gas mode. The use of He and O<sub>2</sub> gas modes may, in some cases, reduce the precision of the analysis but reduces molecular interference and hence improves accuracy. In some cases (e.g. the REEs), the choice of gas mode is recommended to reduce known interferences, whilst for others with similar accuracy and precision between gas modes, a mode is chosen based on the improved accuracy and/or precision. For all three batches, Li, Sc, Ti, Cr, Co, Ni, Cu, Zn, Ga, Ge, Rb, Zr, Cd, Sn, Sb, and Ba were analysed in no gas mode; Mg, V, Mn, Sr, Nb, Y, Mo, Ta, and W were analysed in collisional He gas mode; and the REEs, Te, Se and S were analysed in reactive O<sub>2</sub> mode. Cs and <sup>208</sup>Pb were analysed in No gas and He gas modes, depending on which mode provided the best accuracy and/or precision in that batch.

#### *Thin Section Images and Scanning Electron Microscopy*

Thin-section images were taken using a Zeiss Axioscope in plane-polarised light and crossed-polars to assist interpretation and targeting of mineral phases. Backscatter SEM imaging was undertaken

using a FEI Quanta 650 FEG SEM at the NHM to characterise crystal textures, as well as identify and target zoned crystals for microprobe analysis. Images were taken at a working distance of approximately 10-15 mm, a voltage of 15 kV, a dwell time of approximately 30  $\mu$ s and variable magnification depending on the feature and desired resolution. Lower resolution SEM mosaics were also taken using the FEI MAPS software to assist interpretation and targeting of minerals.

#### *Electron Microprobe Analysis*

Electron microprobe analyses (EMPA) was undertaken on selected samples for major and minor elements using a Cameca SX100 electron microprobe at the NHM, equipped with 5 WDS (wavelength dispersive spectrometers) and 1 EDS (energy dispersive spectrometer), using an electron gun voltage of 20kV and current of 20 nA. A focussed beam of  $\sim$ 2  $\mu$ m was used for pyroxenes and Fe-Ti oxides, 5  $\mu$ m for plagioclase feldspar and 20  $\mu$ m defocussed beam for amphibole and glass (in thin sections). Glassy ash particles, due to their small size and vesicular texture, were analysed using a narrower 10  $\mu$ m defocussed beam to ensure the beam analysed the vesiculated glass. Na was analysed for 10s at the start of each run, followed by 20s for the major and minor elements (Si, Mg, Al, Ca, Ti, Cr, Mn, Fe, Ca and Ni). Detection limits for most elements were < 0.1 wt.%, and standard deviation of the analyses was typically < 0.5 wt.%. Matrix effects were corrected using the Cameca PAP procedure built into the microprobe.

## **4. RESULTS**

### *4.1 Whole-rock geochemistry*

The crystalline pyroclastic, ballistic ejecta and lava samples had <1 wt.% Loss on Ignition (LOI). Only two ash samples had significantly high LOIs (>4 wt.%) and were removed from further study; the remaining ash samples had  $\leq$ 1 wt.% LOI. Most of the samples are medium-K calc-alkaline andesites with 59-62 wt.% SiO<sub>2</sub>. They show considerable overlap with andesites from the 1998-2005 phase and other historical Volcán de Colima andesites (Fig. 3; Luhr, 1992, 1997, 2002; Luhr and Carmichael, 1980, 1990; Luhr and Prestegard, 1988; Luhr et al., 2010; Moorbath et al., 1978; Mora et al., 2002; Reubi and Blundy, 2008; Reubi et al., 2017; Robin et al., 1987, 1991; Saucedo et al., 2010; Savov et al., 2008; Verma and Luhr, 2010). Set against an index of fractionation (whole-rock Mg#,  $Mg\# = [100 \times (Mg/(Mg+Fe_{tot}))]$ ), Al<sub>2</sub>O<sub>3</sub> displays a broadly positive trend with decreasing Mg#, whereas TiO<sub>2</sub> displays a broadly negative trend (Fig.4); however, in both cases most of the data is tightly clustered between Mg# 51-54. This is also shown by limited variation of SiO<sub>2</sub> and with respect to major and minor elements (Supplementary Fig. 1). Most of the trace element compositions, like the major

elements, are tightly clustered; Cr shows a clear negative trend against decreasing Mg# while Sr shows a more scattered trend. Positive yet scattered trends are seen in incompatible elements such as Rb and Zr with decreasing Mg# (Fig. 4).

A time-series of whole-rock compositions throughout the six eruptive phases show that the bulk chemistry of the rocks from the 2013-17 eruption broadly fit in the range of post-1913 (1961-2005) compositions (Fig. 5). As a whole, the data are relatively homogeneous and show little evidence for a significant trend towards more mafic compositions with time. However, whilst Phases 1 and 2 have average compositions that are slightly more evolved than the post-1913 average, there are periods of reversals towards more mafic compositions. Prior to the start of Phase 3, ash and lava samples appear to have slightly reduced SiO<sub>2</sub> content and have a higher Mg# and Cr content. Also notable are the ash samples erupted between the lavas of Phases 4 and 5 which also have a slightly reduced SiO<sub>2</sub> content on average and a higher Mg# and Cr content. PDC clasts from Phase 6, although mostly have a similar SiO<sub>2</sub> content, they have a wide range of Mg# and Cr content. Noteworthy is in the mafic sample from a PDC erupted in 2017 in La Arena ravine, which contains the lowest SiO<sub>2</sub> content (c. 54 wt.%) and the highest whole-rock Mg# (59) and Cr content (c. 200 ppm).

#### *4.2 Petrography and Mineral Chemistry*

The crystalline pyroclastic, ballistic ejecta and lava samples from the 2013-17 eruption are crystal-rich (c. 40-50 vol.%) with porphyritic textures. The phenocrysts are generally plagioclase (25-40 vol.%), orthopyroxene (3-10 vol.%), clinopyroxene (2-8 vol.%), Fe-Ti oxides (1-2 vol.%) and rare amphibole and resorbed olivine ( $\leq 1\%$ ). Glomerocrysts, comprising clinopyroxene + orthopyroxene + plagioclase + Fe-Ti oxides  $\pm$  resorbed olivine, are ubiquitous and often include interstitial glass with meniscus structures and circular plagioclase needles. Similar glomerocrysts or agglomerations of pyroxene + plagioclase + Fe-Ti oxides  $\pm$  olivine have been described by previous authors (Reubi and Blundy, 2008; Saucedo et al., 2010; Crummy et al., 2014) and are a ubiquitous feature of Volcán de Colima andesites. The general mineralogy is similar to that described for the 1998-2005 erupted products (Luhr, 2002; Reubi et al., 2019; Reubi and Blundy, 2008; Savov et al., 2008). Representative mineral chemical compositions for the different mineral phases are shown in Supplementary Table 2.

##### *Plagioclase*

Plagioclase crystals range from large (up to 3 mm) euhedral elongate to tabular phenocrysts to groundmass microlites ( $\leq 30 \mu\text{m}$ ) and also occur as constituents in glomerocrysts (Supplementary Fig. 2A, B). Their compositions typically range between An<sub>40</sub> (Anorthite) to An<sub>80</sub>. Disequilibrium textures include high-An (An<sub>60</sub> - An<sub>80</sub>) sieved cores, infilled with lower-An plagioclase and inclusions; and

dissolution surfaces on low-An ( $An_{40}$  -  $An_{60}$ ) plagioclase mantled by thick higher-An ( $\Delta An > 5$ ) plagioclase. Low-amplitude, high frequency oscillations in anorthite content ( $\Delta An < 5$ ) are ubiquitous in the low-An portions. Groundmass plagioclase crystals typically have compositions of  $An_{30-50}$ .

### *Pyroxenes*

Pyroxenes (orthopyroxene > clinopyroxene) are present as subhedral to euhedral phenocrysts (Fig. 6) (300  $\mu\text{m}$  to 1 mm) and microphenocrysts (30 - 300  $\mu\text{m}$ ) and in glomerocrysts (Fig. 6B). Crystals are often homogeneous, but normal and reverse bands and rims are common. They display a variety of disequilibrium textures and zoning types, including dissolution surfaces, rounded cores, and bands with high Mg# (75-88) and  $\text{Cr}_2\text{O}_3$  (0-1.2 wt.%). Blurred boundaries between zones of contrasting composition are also a common feature among some zoned pyroxene phenocrysts. Orthopyroxene phenocrysts range in composition from Enstatite (En) 60-86 with Mg# of 65-88. Clinopyroxenes are typically augitic, with Wollastonite (Wo) 37-45 and Mg# ranging from 69 to 88. In the low-Mg# 69-76 cores and homogenous crystals, melt and inclusions of Fe-Ti oxides and apatite are relatively common and often align parallel with the crystal edges, particularly for the orthopyroxene. In the more mafic cores and rims, mineral inclusions are absent and melt inclusions are rare. Pyroxenes are also present in the reaction coronae of amphibole and as a minor phase in the groundmass.

On the basis of the textural characteristics, three main types of pyroxenes are recognised irrespective of ortho- or clinopyroxene composition (Tab. 1): 1) homogeneous; 2) normal zoned and 3) reverse zoned.

The most abundant phenocryst type is the Homogeneous type (Fig. 6A), which constitutes most of the microphenocrysts and phenocryst assemblage. It is also abundant in glomerocrysts (Fig. 6B). This type is inclusion-rich with abundant glass, apatite and oxide inclusions, and has a low-Mg# and low  $\text{Cr}_2\text{O}_3$  content with little or no change in Mg# ( $\leq 5$ ) across the crystal.

Normal zoned (NZ) pyroxenes are split into three types according to the chemistry and zoning patterns (Tab. 1; Figs. 7,8). Type 1 (NZ-T1) crystals have a rounded low-Mg# core with inclusions of Fe-Ti oxides and apatite, mantled by dissolution surface and a high-Mg#, high- $\text{Cr}_2\text{O}_3$  band, and rimmed by low-Mg# rim with inclusions near the exterior of the crystal (Fig. 6C, 7A, 8A). The interface between the mafic band and the evolved rim is blurred. Type 2 (NZ-T2) cores have a similar zoning pattern (Fig. 6D, 7B, 8B), but the core itself is more magnesium-rich and mostly lacks the oxide and apatite inclusions in Type 1. Type 3 (NZ-T3) has a high-Mg#, high- $\text{Cr}_2\text{O}_3$  core and a low-Mg# rim (Fig. 6E, 7C, 8C), with an intermediate band between, though this is sometimes obscured by

blurred boundaries between the core and outer zones. All three zoning groups are found within the glomerocrysts, however NZ-T3 type is the most abundant.

Reverse zoned (RZ) phenocrysts display core zoning patterns similar to the normal zoned crystals, but with a characteristic high-Mg# rim (Tab. 1). Type 1 (RZ-T1) has an inclusion-rich, low-Mg# and low-Cr<sub>2</sub>O<sub>3</sub> core, mantled by the high-Mg rim (Fig. 6F, 7D, 8D). Type 2 (RZ-T2) is similar to the normal zoned Type 2, with an intermediate core, mantled by an inner high-Mg# band, an outer low-Mg# band, and the final high-Mg# rim (Fig. 7E, 8E). Type 3 (RZ-T3) has a high-Mg#, high-Cr core mantled by an evolved band, and rimmed by high-Mg# rim of this type (Fig. 7F, 8F).

The presence of normal zoned crystals has been documented by Koubi and Blundy (2008) in the 1999-2005 lavas. In contrast, reverse zoning is a common feature for pyroxene of Plinian deposits (Crummy et al., 2014; Luhr et al., 2010; Luhr and Carmichael, 1982), but a rare occurrence in interplinian products (various units to 1975-76, Luhr and Carmichael, 1980; 1998-99 lavas, Mora et al., 2002). This is in contrast with our observation of the abundance of RZ crystals in 2013-2017 products.

#### *Amphibole*

Amphibole phenocrysts are rare (< 1 vol.%) with typically 1-3 large phenocrysts (0.5-4.0 mm) per thin section. They show extensive reaction rims of pyroxenes, plagioclase, oxides and interstitial glass (Supplementary Fig. 2). Amphibole phenocrysts are magnesiohastingsites and Ti-rich magnesiohastingsite in composition (Loake et al., 1997; Hawthorne et al., 2012). All amphiboles have resorbed textures (rounded crystal edges in larger amphiboles and small rounded amphibole crystals) and have either opacitic or coarse-grained reaction rims, as noted in 1998-99 and earlier samples (Luhr, 2002; Macías et al., 2017). Crystals displaying opacitic rims are typically rounded, subhedral amphiboles with phenocryst reaction rims composed of fine-grained pyroxenes and oxides, often displaying as a black rim in PPL (Supplementary Fig. 2C). These amphiboles are typically smaller than the other type, and the thickness of the reaction rim ranges from 50 µm to, in rare cases, a completely altered fine-grained pseudomorph. In contrast, the coarse-grained type of reaction rims has extensive resorption of the crystal, forming remnant anhedral amphibole crystals and a thick reaction rim of fine to medium grained pyroxene, plagioclase and Fe-Ti oxide crystals (Supplementary Fig. 2D). In some cases, finer crystals of this assemblage are present rimmed by larger phenocrysts of pyroxene and plagioclase indicating these crystal assemblages may be pseudomorphs of former, reacted-out amphibole.

#### *Fe-Ti Oxide*

Fe-Ti oxides are ubiquitous as microphenocrysts (50-250  $\mu\text{m}$ ), either isolated or in glomerocrysts. They also occur as small inclusions within pyroxenes and plagioclase, and in the groundmass. Small crystals also occur as reaction products in olivine coronae and amphibole reaction rims (Supplementary Fig. 2E). All the oxides found in this study are titanomagnetite. Ilmenites, though common at other arc volcanic systems, were not found in this study and are thought to be relatively rare in interplinian Volcán de Colima andesites (Reubi and Blundy, 2008; Mora et al., 2002).

#### *Olivine*

Olivine phenocrysts are exclusively present as anhedral, heavily resorbed and embayed phenocrysts (300-600  $\mu\text{m}$ ) and range in composition from Forsterite (Fo) 68 to 77. They are surrounded by coronae of orthopyroxene and peritectic/symplectitic overgrowths of Fe-Ti oxides at the boundary between the olivine and orthopyroxene crystals (Supplementary Fig. 2F). These peritectic/symplectitic Fe-Ti oxides have a 'wormy' texture, distinct from the blocky or rounded oxide inclusions seen in pyroxenes not associated with olivine, and can be used to discriminate between orthopyroxenes crystallised from melt and reacted-out olivines. These corona-rimmed olivine phenocrysts can occur individually or as part of a larger glomerocryst.

#### *Groundmass*

The groundmass comprises small ( $\leq 300 \mu\text{m}$ ) plagioclase, orthopyroxene and Fe-Ti oxide crystals, with abundant glass and very minor clinopyroxene. Groundmass crystals range from euhedral, blocky/prismatic to acicular plagioclase needles and euhedral, blocky to elongate orthopyroxene microlites.

#### *Glass*

Groundmass and ash glass compositions for Volcán de Colima samples are much more evolved than the bulk rock (60-79 wt.%  $\text{SiO}_2$ , Supplementary Fig. 3), consistent with previous studies of ash and groundmass glasses and melt inclusions (Luhr, 2002; Mora et al., 2002; Atlas et al., 2006; Luhr, 2006; Reubi and Blundy, 2008; Cassidy et al., 2015; Reubi et al., 2013). Groundmass glass and interstitial glass in glomerocrysts are the most differentiated, with high  $\text{SiO}_2$  (65-79 wt.%) and  $\text{K}_2\text{O}$  (2-4 wt.%) contents and low MgO (typically  $<1$  wt.%) contents. Glassy inclusions in pyroxenes and plagioclases broadly overlap with the composition of groundmass glass and interstitial glass in glomerocrysts. Plagioclase-hosted glass inclusions typically range between 67-77 wt.%  $\text{SiO}_2$ , with inclusions within sieve-textured cores less evolved (67-73 wt.%  $\text{SiO}_2$ ). Pyroxene-hosted inclusions vary depending on the zoning type, with inclusions in Homogeneous and NZ-T1 cores having  $\text{SiO}_2$  contents up to 76

wt.%, but inclusions on the band-rim boundaries and rims of NZ-T2 and NZ-T3 types between 66-71.5 wt.% SiO<sub>2</sub> and lower K<sub>2</sub>O contents (2.0-2.6 wt.%). Though melt inclusions are not the focus of this study, these compositions do broadly agree with compositions in other studies (Atlas et al., 2006; Reubi and Blundy, 2008; Reubi et al., 2013) and indicate more evolved melt compositions when crystallising the lowest Mg# pyroxene crystal rims.

Analyses of glass from ash fragments were undertaken on small, highly-vesiculated shards as these are more likely to represent vapour-saturated melt prior to eruption rather than fragments of partially degassed and evolved conduit material and dome rock, akin to the 'vesicular' and 'dense' fragment types of Cassidy et al. (2015). Although the analyses show a considerable spread in composition, 60-77 wt.% SiO<sub>2</sub>, they are on average the least evolved glass compositions (two-thirds less than 68 wt.% SiO<sub>2</sub>) and have intermediate composition between the whole-rock and the groundmass glass.

## 5. CRYSTALLISATION CONDITIONS

### *Temperature*

The pre-eruptive conditions (temperature, pressure, oxygen fugacity) can be constrained using mineral-mineral and mineral-melt thermobarometers (e.g. Wells, 1977; Andersen et al., 1993; Putirka, 2008; Ridolfi et al., 2010; Neave and Putirka, 2017), which require equilibrium between the two components (i.e., mineral-mineral or the mineral-melt) (Putirka, 2008). Since the equilibrium can be tested only between rims of co-existing minerals or between rim and melt, only pre-eruptive intensive variable can be usually constrained (e.g. Putirka, 2008). As previously discussed, the melt compositions here are so evolved that mineral-melt equilibrium for either clinopyroxene-melt and orthopyroxene-melt geothermometers is unlikely, especially for the high-Mg# rims. The mixing and mingling of compositionally different melts and crystals in the magmatic system can also significantly affect the equilibrium mineral-melt, and minerals can be in equilibrium with a melt of different composition from the residual groundmass liquid.

To overcome this problem, we employ the approach of Mangler et al. (2020) using the two-pyroxene thermobarometer of Putirka (2008). One requirement of this type of thermobarometer is that the two pyroxenes should be touching, as this implies co-crystallisation. However, pyroxenes may be remobilised and mixed at any point during growth to eruption in magmatic systems, as is attested by complex disequilibrium and remobilisation textures widely found in crystals. The similar Mg# and identical inclusion, zoning and textural patterns strongly suggest that both orthopyroxene and clinopyroxene in Volcán de Colima magmas co-crystallised under the same conditions. This suggests

that, although the pyroxene portions are not touching, they probably co-crystallised under the same conditions through the crystallisation sequence. By crossing the entire orthopyroxene data ( $n = 1513$  points) set against the entire clinopyroxene dataset ( $n = 1334$  points), we were able to estimate temperature and pressure from pairs in Fe-Mg equilibrium ( $K_D(\text{Fe-Mg})^{\text{cpx-opx}} = 1.09 \pm 0.14$ ; Putirka, 2008). This method provides a larger data set of temperature and pressure estimates of pre-eruptive condition, a better statistical basis for interpretation, and can reduce relatively large model error of the temperature estimate (from  $\pm 45$  in the original model to  $\pm 18^\circ\text{C}$ ).

The results of the modelling for individual points are shown in Figure 9, organised by pyroxene type. Temperatures of the evolved NZ-T1 cores and rims, NZ-T2 and NZ-T3 rims are estimated at approximately  $980\text{-}1010^\circ\text{C}$ , and the intermediate cores of NZ-T2 are estimated at between  $1000\text{-}1030^\circ\text{C}$ . The mafic bands in both of these types have temperatures on average  $1030\text{-}1040^\circ\text{C}$ , similar to the average temperature of NZ-T3 mafic cores. Homogeneous crystals record a temperature of c.  $980^\circ\text{C}$ , overlapping with the evolved NZ composition and in agreement with their petrography. Similarly, low-Mg# compositional zones of reverse zoned crystals have temperatures ranging in the same interval: RZ-T1 cores,  $980\text{-}1000^\circ\text{C}$ ; RZ-T2 low-Mg# bands,  $990\text{-}1000^\circ\text{C}$ ; and RZ-T3 low-Mg# bands,  $980\text{-}1000^\circ\text{C}$ . The more mafic portions (high-Mg#) internal portions of RZ-T2 have temperature of  $995^\circ\text{C}$ , slightly lower than  $\text{Mg}^{2+}$  equivalent; and the high-Mg# core of RZ-T3 record temperatures of  $1010\text{-}1040^\circ\text{C}$ . For all three RZ types, the mafic rims have temperature estimates between  $1010\text{-}1050^\circ\text{C}$ , averaging at between  $1020\text{-}1030^\circ$  ( $\pm 18^\circ\text{C}$ ).

When considering these temperatures all together, we can define a calibration curve of temperature vs pyroxene compositions (i.e. Mg#) (Fig. 10). We can also define at least two end-members: a mafic (high-Mg#,  $\text{Mg\#} > 77$ ) and evolved (low-Mg#,  $\text{Mg\#} 69\text{-}75$ ) member. These show that the average temperatures for the evolved end-member is typically between  $980\text{-}1000^\circ\text{C}$ , and the mafic end-member is estimated to have a relatively wide range, but typically between c.  $1020\text{-}1080^\circ\text{C}$ . Temperature estimates from this study agree well with those from previous studies (Luhr and Carmichael, 1980; Luhr, 2002; Mora et al., 2002; Luhr and Carmichael, 1990; Reubi and Blundy, 2008; Savov et al., 2008; Crummy et al., 2014; Cassidy et al., 2015), although we note that the temperature estimates for the highest Mg# are slightly lower than previous estimates by Reubi and Blundy (2008). This may potentially be due to small amounts of mixing with more evolved melt during injection and crystallisation of mafic bands and rims. Experimental data by Moore and Carmichael (1998) also give temperatures of  $950\text{-}978^\circ\text{C}$  for the most evolved rocks, within error of the estimates reported here for the most evolved pyroxene compositions. However, it is the first time that a calibration curve of



temperature has been proposed to encompass the whole range of variability of pyroxene compositions.

Whilst thermobarometric estimates from pyroxene are the main focus of this study, supplementary information using amphibole compositions and apatite saturation temperatures can aid interpretation of crystallisation conditions. The Al-in-amphibole model of Ridolfi et al. (2010) suggest crystallisation temperatures of c. 930-1000°C and 2.9-5.0 kbar pressure for the amphiboles (Supplementary Fig. 4). Apatite saturation temperatures, using SiO<sub>2</sub> and P<sub>2</sub>O<sub>5</sub> content from whole-rock compositions and using the method of Piccoli and Candela (1994), suggest apatite saturation at 930-950°C (Supplementary Tab. 3). These temperatures are cooler than those estimated from the two-pyroxene thermometry and rely on less reliable parameters (whole-rock composition), but are within the errors of the thermometry model and overlap with apatite crystallisation predicted by MELTS modelling. Together, these support the interpretation of the presence a cooler evolved end-member.

#### *Pressure*

Pressure estimates using the two-pyroxene thermobarometer (Putirka, 2008) using the same method as above, show consistent estimates between 1.9 to 7.5 kbar (Fig. 11) ( $\pm 2.8$  kbar, as per Putirka, 2008), with average pressure estimates for all groups and zones between 4 and 6 kbar. Using the few equilibrium clinopyroxene melt pairs available, we also compared the performance of the two-pyroxene method to clinopyroxene-liquid and clinopyroxene-only thermobarometers of Putirka (2008) (Supplementary Doc. 1 and Supplementary Tab. 4). The results show good agreement with the estimates calculated with the two-pyroxene method and are therefore considered to be reasonable when considering the model error.

Pressure estimates from amphibole geobarometry indicate crystallisation pressures of 2.9-5.0 kbar (Ridolfi et al., 2010; Supplementary Fig. 4). However, pressure estimates using the Ridolfi et al. (2010) model can be influenced by melt compositions (Erdmann et al., 2014) and as such these estimates should be treated with caution, even if they agree with the pyroxene-based thermobarometry.

#### *Oxidation State*

Estimates of the oxidation state of the magmas have been made in previous studies using two-oxide oxythermometry using the method of Andersen and Lindsley (1988). Ilmenites are rare in Volcán de Colima magmas, and touching pairs of ilmenite and magnetite are very rare. Estimates vary between  $\log f_{O_2}$  -11.4 to -9.2 depending on the method used (Mora et al., 2002; Reubi and Blundy,

2008; Luhr and Carmichael, 1980). Whilst no ilmenite was found in this study to give a comparative constraint, these values are broadly in agreement with estimates using the amphibole-based model of Ridolfi et al. (2010) ( $\log f_{O_2}$  -10.5 to -9.5;  $\sim NNO+1$ ; Supplementary Fig. 4).

## 6. DISCUSSION

### 6.1 Paragenesis

The 2013-2017 eruptive phase at Volcán de Colima is characterised by andesites with a very restricted range of whole-rock compositional variability (Figs. 3, 4, 5), similar in many respects to the preceding 1998-2011 interplinian phase (Luhr, 2002; Mora et al., 2002; Reubi and Blundy, 2008; Savov et al., 2008). All samples contain plagioclase + orthopyroxene + clinopyroxene + Fe-Ti oxides, along with residual groundmass glass, amphibole with reaction rims, antecrystic resorbed olivine, and glomerocrysts of the main crystallising phases. Petrographic and textural evidence suggests a general crystallisation sequence of antecrystic olivine  $\rightarrow$  high-Mg# clinopyroxene + high-Mg# orthopyroxene + high-An plag + oxide (in glomerocrysts)  $\pm$  amphibole  $\rightarrow$  low-Mg# clinopyroxene + low-Mg# orthopyroxene + plag + oxide  $\pm$  amphibole  $\rightarrow$  low-Mg# orthopyroxene + plag + apatite  $\pm$  low-Mg# clinopyroxene.

However, whole-rock compositions and textural evidence also suggest significant disequilibrium. Fractionation modelling of whole-rock compositions have failed to replicate the bulk composition of these rocks at Volcán de Colima, notably that MgO content recorded in the bulk rock is higher than that generated only by fractional crystallisation from a mafic parent (Supplementary Fig. 5). This observation was also noted for the 1998-2005 rocks by Reubi and Blundy (2008). Textural information recorded in the dissolution/resorption surfaces and zoning profiles of crystals also indicate significant disequilibrium and crystallisation in different magmatic environments, suggesting mixing of magmas and remobilisation of crystals.

The restricted range of whole-rock compositions suggests that these mixing processes are efficient and buffer the whole-rock compositions from large chemical variations. While there appears to be increases in whole-rock Mg# (outside the range of error) in some ash samples from Phases 4 and 5 (2015-16,  $\Delta Mg\# \sim 4$ , Fig. 5) and some fluctuation toward the end of Phase 2 and initial phase 4, these correlate with only moderate decreases in  $SiO_2$  and moderate increases in whole-rock Cr content. When plotted on a mixing line between the average whole-rock composition and a mafic component (the proposed parental magma for the Colima magmatic system, using magma composition SAY-22E from Luhr and Carmichael, 1981; or a homogenised gabbroic fragment from Reubi and Blundy, 2008), the 2015-16 ash samples clearly lie on a trend towards

clinopyroxene+orthopyroxene and not towards the mixing trend with the mafic component (Supplementary Fig. 6). This trend may be explained by these particular samples being more crystal-rich (and/or glass-poor) compared to other samples, and the trend may be accounted for by accumulation of clinopyroxene and orthopyroxene crystals of  $\leq 10\%$  clinopyroxene+orthopyroxene (Supplementary Fig. 6). Similarly, some ash samples from Phase 3 have anomalously low MgO, which may be due to the opposite effect of these samples being relatively crystal-poor and/or glass-rich, unrelated to simple mixing with the mafic components. Much greater changes in bulk composition, notably SiO<sub>2</sub>, would be expected for a reversal to more mafic bulk compositions of the erupted products.

In contrast, our mafic sample (COL-PF17/007A-CIIV) from the 2017 PLC deposit in La Arena ravine (Fig. 5), is much more mafic (54 wt.% SiO<sub>2</sub>, Mg# 59) and plots on a mixing line between 'average' whole-rock compositions in this study and the proposed mafic parental magmas (Supplementary Fig. 6). Petrographically, however, this sample contains embayed olivines without the peritectic orthopyroxene overgrowths seen in all the other samples, and is much more akin to the prehistoric 'olivine andesites' (i.e., samples Col-9 and Col-11) of Luhr and Carmichael (1980). As this particular clast was obtained from a pyroclastic flow deposit, this sample may be a remobilised fragment of a similar lava flow to the olivine andesites of Luhr and Carmichael (1980) and possibly unrelated to the present activity at Volcán de Colima. Whilst this sample may be petrogenetically useful, representing a potential spectrum of the Volcán de Colima mafic end-member, it is unlikely to be representative of the current state of the magmatic environments recorded in the chemistry and petrology of the other samples.

## 6.2 Magmatic environments

Clear evidence of magma mixing is revealed by the complex chemical composition, zoning and textures of the crystal cargo, that suggest an active system defined by disequilibrium and mixing of different melts and growth and storage in compositionally distinct magmatic environments.

In particular, pyroxene composition and textures allow us to recognise at least two magmatic environments. Based on the low-Mg#, very low Cr<sub>2</sub>O<sub>3</sub> compositions (< 0.1 wt.%), and inclusions of phases such as apatite and abundant Fe-Ti oxides, the Homogeneous type crystallised from a relatively evolved magma end-member, saturated with respect to apatite and Fe-Ti oxides, alongside plagioclase of An<sub>40</sub> to An<sub>60</sub>. NZ-T1 and RZ-T1 crystal's cores with low-Mg# and rich in inclusions (including abundant glassy inclusions, which may indicate pervasive resorption), also suggests crystallisation from this evolved magmatic environment, alongside the evolved rims of NZ crystals

(Figs. 7,8; Tab. 1). Due to the abundance of the Homogeneous crystal type (> 60% phenocrysts and > 80% microphenocrysts) and the frequency of low-Mg# composition, the evolved magmatic end-member is considered to be dominant in the magmatic system, consistent with the homogeneous 'weakly-zoned' crystals (Reubi and Blundy, 2008) considered the primary crystallising phase for the evolved magmas at Volcán de Colima from previous studies (Reubi and Blundy, 2008; Savov et al., 2008; Mora et al., 2002). Our thermometry estimates indicate a temperature of c. 980-1000°C ± 18°C for this magmatic environment.

By contrast, the rims of RZ crystals, cores of RZ-T3 and NZ-T3, bands and some cores of NZ-T2, alongside bands of NZ-T1 and RZ-T2 are comparatively mafic, with high Mg# and Cr<sub>2</sub>O<sub>3</sub> contents (Figs. 7, 8; Tab. 1), and represents a second separate mafic magmatic environment, constrained at a temperature of c.1020-1040°C ± 18°C using the two-pyroxene geothermometer. Other mineral phases co-crystallising in this environment are high-anorthite (An<sub>60</sub>-An<sub>80</sub>) plagioclase and oxides, and may be associated with olivine, although there are no clear evidence that it is crystallising in this environment. Cores in NZ-T1 and -T2 are often rounded and bounded by resorption surfaces, and are mantled by bands with the highest Mg# and Cr<sub>2</sub>O<sub>3</sub> content suggesting mixing between the evolved and mafic end-members upon heating and dissolution of the evolved cores during entrainment and crystallisation of mafic bands.

To summarise, we suggest that at least two dominant magmatic environments are present in the plumbing system at Volcán de Colima: (1) An evolved magmatic environment (hereafter also defined as low-Mg#), crystallising low Mg# orthopyroxene and clinopyroxene (Mg# 69-75), An<sub>40-60</sub> plagioclase, amphibole, and saturated in Fe-Ti oxide and apatite at 980-1000°C, and (2) a mafic magmatic environment (hereafter also defined as high-Mg#), crystallising high-Mg# (77-89) and high-Cr<sub>2</sub>O<sub>3</sub> (0.2-1.2 wt.%) pyroxene, high An (An<sub>60</sub> to An<sub>80</sub>) plagioclase and olivine at 1020-1080°C. Assessing the mantle source of these melts is out of the scope of this paper, however we speculate that the original source of the mafic melts may be parental basaltic melts (Luhr and Carmichael, 1981; Carmichael et al., 2006; Verma and Luhr, 2010), which are compositionally similar to the compositions of the gabbroic clots of Reubi and Blundy (2008). A possible third, intermediate magmatic environment crystallising pyroxene of (Mg# 74-84) and plagioclase, which only occurs as cores of NZ-T2 and RZ-T2 crystals, and mostly lacks any inclusions typical of the evolved type cores, may be present. Alternatively, this intermediate zoning types may be explained by long-term storage and diffusive re-equilibration of mafic crystals in an evolved melt environment as recently described in the Popocatepetl volcanic system by Mangler et al. (2020).

### 6.3 Magma mixing dynamics

The variety of chemistry and textures of minerals observed in this study, clearly indicates that magma dynamics at Volcán de Colima is influenced by magma mixing processes between mafic and evolved magmatic end-members leading to a complex interplay between the different magmatic environments. A summary of the magmatic end-members and their relation to crystal textures is shown as the schematic Figure 12 and the petrological model Figure 13.

Within the mafic magmatic end-member, high-Mg# pyroxenes crystallise alongside olivine and high-An plagioclase. Injection of melts from the mafic end-member remobilises these crystals, and the mafic magmas migrate into the reservoirs hosting the evolved end-member magmas. These injections remobilise the high-Mg# pyroxenes and associated crystals (e.g. cores of NZ-T3) of the mafic end-member, and can therefore be considered antecrysts when injected in the evolved reservoir (e.g. Davidson et al., 2007). These recharge events not only remobilise and entrain mafic crystals, but also remobilise resident evolved crystals (e.g. cores of NZ-T1) and partially re-equilibrated mafic crystals from previous recharge events (e.g. cores of NZ-T2), both already present within the evolved end-member. The injection and entrainment by the mafic melt in this reservoir causes heating and disequilibrium conditions, and results in resorption of extant pyroxene cores followed by the formation of a high-Mg# and high-Cr band (Fig. 12). Entrainment also results in pervasive resorption and sieve textures in plagioclase, as the high-An portion dissolves and lower-An plagioclase from the evolved end-member infills the voids (Streck, 2008). Olivine phenocrysts, which may have been stable in the high-temperature mafic environment, begin to break down in the new magma forming peritectic coronae.

The formation of the high-Mg# and high-Cr band around the evolved (NZ-T1), partially re-equilibrated (NZ-T2) and mafic antecrystic cores (NZ-T3) is a result of crystallising from an initially more mafic melt. As mixing proceeds, following a process of efficient mixing as seen at other volcanoes (e.g. Popocatepetl, Mangler et al., 2020; Stromboli, Petrone et al., 2018), the magmatic environment around the crystal changes from mafic to the evolved composition, reflecting the chemistry of the resident magma. In most cases this results in the formation of an evolved rim, but in rare cases homogenisation and fractionation may occur as the magma evolve towards the evolved end-member, capturing the on-going mixing (Petrone et al., 2018). Within this evolved end-member, low-Mg# pyroxene and low-An plagioclase crystallise along with saturation and crystallisation of Fe-Ti oxide and apatite (the latter present as inclusions). Storage in the evolved end-member results in growth of low-Mg# rims of the NZ-type crystals, along with the indigenous Homogeneous type crystals. These crystals may stall and develop blurry zone interfaces by diffusion before being remobilised by a later mafic injection shortly before eruption.

Small-scale local variations in crystallisation conditions (temperature, pressure, volatile content etc) lead to low-amplitude, high frequency oscillations in anorthite content ( $\Delta An < 5$ ) textures which are abundant in plagioclase (Streck, 2008; Ginibre et al., 2002).

Subsequent mafic injections may either result in the same processes, forming additional mafic bands, or may trigger or prime the system for eruption, resulting in the crystallisation of a final mafic rim in pyroxene (e.g. RZ-type crystals). In plagioclase, the presence of dissolution surfaces typically on low-An ( $An_{40}$  to  $An_{60}$ ) portions mantled by thick higher-An ( $\Delta An > 5$ ) bands are evidence of these later injections of hotter magmas and dissolution of the resident low-An plagioclase (Ginibre et al., 2002; Streck, 2008).

Finally, these phenocryst-bearing magmas rise towards the surface, crystallising dominantly-evolved microphenocrysts and groundmass in shallow storage regions and as they rise through the conduit and erupt (Reubi and Blundy, 2008; Savov et al., 2008; Reubi et al., 2013; Cassidy et al., 2015). Amphibole phenocrysts, which may have been stable at depth in the plumbing system (Moore and Carmichael, 1998; Macías et al., 2017; Crummy et al., 2014; Reubi and Blundy, 2008) encounter disequilibrium conditions during storage and ascent and result in the formation of reaction rims (Rutherford and Hill, 1993; Rutherford and Devine, 2003; Macías et al., 2017).

Given the similarities between the zoned textures of glomerocryst and free crystals, we interpret that the glomerocrysts and remnant amphibole and olivine represent fragments of the mush remobilised during recharge events and portions of free crystals represent disaggregated parts of these agglomerations.

Geophysical studies have indicated that a significant low velocity zone (LVZ) is present beneath the volcano and that most of this body is liquid (Spica et al., 2017; Sychev et al., 2019). The textural and chemical evidence from this study is consistent with a semi-molten, mushy magma body beneath the volcano (Fig. 13). Geothermobarometry estimates for the pre-eruptive conditions also suggest that these crystals form at overlapping depths with the proposed LVZ. In fact, our observations of a complex variety of the crystal types, suggests repeated growth, storage, remobilisation and disaggregation in an heterogeneous mush, is consistent with the model of small, ephemeral amounts of mafic melt passing through a semi-crystalline, mostly evolved body via conduits to small reservoirs (Atlas et al., 2006; Reubi et al., 2013; Reubi et al., 2015).

Such structures of small ephemeral reservoirs within a subsolidus mush are recognised as a common feature at many volcanic systems (Cashman et al., 2017; Edmonds et al., 2019). For example, within the TMVB, Mangler et al. (2020) describe similar populations of crystals reflecting homogenisation

processes and remobilisation of older crystalline material within the volcanic plumbing system of Popocatepetl, along with storage zones in the mid and upper crust. Wallace et al. (2020) and Scott et al. (2013) interpret plagioclase textures and mineral chemistry in rocks erupted at Santiaguillo, Guatemala, as representing mixing between more and less evolved melts within a chemically stratified mush zone; with ascent of these magmas remobilising previously crystallised portions of the crystal mush. Similar processes of mafic recharge, remobilisation, mixing and homogenisation within trans-crustal mush systems have also been described in the Tongariro Volcanic Centre in New Zealand by Kilgour et al. (2014), Coote and Shane (2016) and Shane et al. (2019). Crystal-rich andesites at volcanoes in other continental arcs, e.g. Cascades volcanoes such as Mount St. Helens (Kiser et al., 2016; Wanke et al., 2019) and Mound Hood (Koleszar et al., 2012), similarly record patterns of mixing, homogenisation and remobilisation in a polybaric plumbing system, as do island arc volcanoes such as Santorini (Fabbro et al. 2017), Soufrière Hills (Paulatto et al., 2019), or Methana in the Aegean arc (Popa et al., 2019; 2020).

#### *6.4 Storage depths and reconciling depth estimates*

Pressure estimates from two-pyroxene barometry suggest that most of the crystallisation occurs between 4-6 kbar, or 12-18 km depth. Given that the thickness of the crust beneath Volcán de Colima is 30-35 km thick (Wallace and Carmichael, 1999; Spica et al., 2017), this places most of the crystallisation of complex zoned crystals and hence mixing and remobilisation, in the mid-crust. These estimates conflict with studies based on melt inclusions, which consistently show melt inclusion entrapment depths in vapour saturated conditions of typically < 8 km for interplinian activity (Atlas et al., 2006; Reubi and Blundy, 2008; Reubi et al., 2013). Experimental data also indicates a shallow (0.7-1.5 kbar) rather than deep storage (Moore and Carmichael, 1998).

The reason for this discrepancy may be due to the large errors inherent with geobarometry tools, in particular the  $\pm 2.8$  kbar model error for two-pyroxene model Equation 39 of Putirka (2008). If an average pressure of 5 kbar is used, the ranges up to 1.8 kbar and near to the upper limit of estimated entrapment pressures. Nevertheless, this highlights the inherent uncertainty in the technique for estimating pressure. Melt inclusions themselves also have limitations, as they may record where the inclusions were sealed rather than the entire crystallisation sequence and are also prone to re-equilibration and other effects (Kent, 2008). In particular Reubi et al. (2013) have suggested that the crystallisation level estimated by inclusions may in fact represent a shallow storage level of the magmatic system, where melt inclusions re-equilibrate, giving instead a final storage level before eruption. Whilst upper to mid-crustal reservoirs in this context may be vertically extensive (e.g. Sychev et al., 2019 at Colima; Kiser et al., 2016 for Mount St. Helens), it is clear that

the pressure estimates of magma batches need to be better constrained at Volcán de Colima for a more complete picture of the plumbing system processes.

Geophysical constraints on the magmatic system also present an unclear picture. Seismic data such as volcano tectonic seismic swarms (Núñez-Cornú et al., 1994; Zobin et al., 2002) and the hypocentres of long period seismic events (Petrosino et al., 2011) have been used as evidence to pinpoint the crystallisation of the hosts and sealing of the inclusions, at depths of between 0.5 to 8.5 km and 1.2 to 4 km depth (Zobin et al. 2002, Núñez-Cornú et al., 1994; Petrosino et al., 2011). These depths have been proposed as approximate levels where magmas ascend, degass and crystallise from a volatile-saturated magma in the subvolcanic storage region or shallow reservoir. However, ambient noise tomography has shown a clear low-velocity body at c. 15 km beneath the volcano, interpreted to be a partially crystallised magma mush zone with small pockets of interconnected melt-rich reservoirs (Spica et al., 2017). Sychev et al. (2013) using similar methods corroborated these interpretations, and added that mixing between melts of contrasting compositions is likely to occur in the mid-crust prior to migration to a 'spongy' shallow magma reservoir. These are in close agreement with the petrological and thermobarometric interpretations of this study, which indicates magma mixing, crystallisation and remobilisation at c. 5 kbar or 15 km depth in the mid-crust (Fig. 13).

Discrepancy between melt inclusion and geobarometric-derived crystallisation pressures and depths is noted at other arc volcanoes. Fractionation at relatively low entrapment pressures has also been noted for Popocatepetl (Atlas et al., 2006), however Mangler et al. (2020) using the same method as this study describe deeper crystallisation in the upper to mid-crust. Studies on the Ruapehu magmatic system in New Zealand have also reported different storage pressures and depths using melt inclusions and geobarometers. Kilgour et al. (2014) reported melt inclusion entrapment pressures of 0.5-3 kbar and depths of c. 2-9 km; whereas mineral-based geobarometry estimates by Conway et al. (2020) report pressures of 3.6 kbar and depths of c. 13 km. These studies highlight that differences in pressure and depths of crystallisation can be obtained using different methods, which can have a significant influence on the interpretation of the magmatic system.

It is possible that the depth estimates record different processes and polybaric crystallisation (e.g. Santiaguito; Wallace et al., 2020). Spica et al. (2017) note that whilst the low-velocity body is present in the mid-crust, magma storage may occur at shallower depths, which correspond to entrapment depths by Reubi and Blundy (2008), Reubi et al. (2013) and other studies. As noted these studies in particular have focused on the 'true phenocrysts' and may have overlooked the 'complexly-zoned' phenocrysts, potentially overlooking information relating to the deeper system by focussing on the



latest, degassing-related crystallisation in the shallow reservoir(s). Reubi et al. (2017) cite the young crystal ages (< 8500 years) for oscillatory-zoned plagioclase crystals as evidence against a protracted, cold-storage type mushy system at Volcán de Colima (e.g. Cooper and Kent, 2014); whilst the ‘antecrystic’ high-An plagioclase are considered outliers, similar to the high-Mg# pyroxenes. These observations may be reconciled by a polybaric magma storage system where injection, mixing and remobilisation occurs extensively in the reservoirs of the deeper mushy storage region, before being transported to shallower depths inducing degassing-crystallisation as indicated by melt inclusion studies. Whilst the mechanics of magma movement through and interaction with crystal mushes is widely debated (Bergantz et al., 2015; Edmonds et al., 2019), a persistently active volcano such as Volcán de Colima with young crystal ages may be explained by a particularly active mush system, with melts and magmas being transported, crystallised and erupted relatively efficiently and at a high flux, and kept at a relatively high temperature. As noted by Reubi et al. (2019), this may indicate that Volcán de Colima is a possible hyperactive ‘end-member scenario’ for these types of systems.

#### *6.5 Mafic injections during the 2013-17 eruption*

Much like the 2005 event (Varley, 2019), the intense 2015 eruption prompted concerns of an increase in activity towards a major Plinian event (Capra et al., 2016; Macías et al., 2017; Reubi et al., 2019). The cause of the event is uncertain, but it has been suggested that it was related to the arrival of a new batch of gas-rich magma in the upper conduit, which erupted as a series of pulses (Reyes-Dávila et al., 2016; Capra et al., 2016).

The arrival of new, mafic magma in the plumbing system would supply additional heat and possibly volatiles, and could drive more intense eruptions. Such an event could be recorded in the crystal cargo by an increase in the number of reverse zoned crystals in the erupted products following the eruption. Point counts of the pyroxene crystal types suggest that in Phases 1 and 2, prior to the 2015 eruption, few reverse zoned crystals were encountered ( $\leq 3\%$  of total crystals). Following the eruption in July 2015, reverse zoned crystals become more common in Phases 4 and 5 (increasing to 10% of the crystal population), and supports the idea of increased injection and mixing of a mafic magma priming or even triggering larger eruptions during interplinian periods.

However, whilst mafic recharge is considered to be a key factor in the timing and influencing the style of volcanic eruptions, other factors such as ascent rate (Cassidy et al., 2015; 2018), the thermal regime of the reservoirs (Ruprecht and Bachmann, 2010); the rheological state of the reservoir (Kozono and Koyaguchi, 2009; Koleszar et al., 2012; Cashman et al., 2017), and the crystallinity and volatile behaviour in the reservoir (Popa et al., 2019; 2020) can modify the influence of mafic

recharge and how an eruption proceeds. For example, whilst it is often considered that fresh undegassed mafic magma may act more explosively as it reaches shallower reservoirs, the additional heat may reduce the viscosity of the magma allowing for more efficient degassing (Ruprecht and Bachmann, 2010; Koleszar et al., 2012); and a higher crystallinity may slow ascent rates facilitating degassing and lowering explosivity (Popa et al., 2019; 2020), resulting in effusive eruptions from high-volatile content magmas. These examples highlight how interpretations of processes following recharge should be mindful of complex interactions in the plumbing system. Accurately constraining magmatic volatile contents, careful modelling, and an understanding of the timescales of magmatic processes will provide the more accurate picture of the plumbing system.

A comparable increase in the proportion of reverse-zoned crystals was observed, although not described quantitatively, at the start of the eruptive phase in 1929-39 (Luhr, 2002). This perhaps indicates that magma mixing triggered the onset of the eruptive phase in 1998 and concurs with our observations for the 10-11 July 2015 event. Our data further suggests that small injections, with little change to bulk chemistry, might be a common process in triggering the start of interplinian eruptive phases in agreement with previous authors (Macías et al., 2017; Reubi et al., 2019).

#### *6.6 The July 2015 eruption and cycle-ending eruptions at Volcán de Colima*

Luhr (2002) suggested that the future event that will terminate this current cycle may not be as intense as the 1913 Plinian eruption, based on the lack of non-destabilised amphibole and lower plagioclase contents observed in the magmas from the current cycle compared to those erupted leading up to 1913. Given the intensity of the July 2015 event and the length and volume of the emplaced PDCs, comparisons could be made between the 2015 event and the 1913 or 1818 Plinian eruption itself; and whether the July 2015 eruption may in fact represent a possible smaller end-cycle event than previous Plinian events. However, based on the findings presented in this study, the evidence does not appear to support this hypothesis.

Firstly, no non-destabilised amphibole crystals (i.e. lacking reaction rims) were found in these rocks, which are abundant in the erupted material from the Plinian eruptions, and this finding is in agreement with descriptions by Capra et al. (2016) and Reyes-Dávila et al. (2016). However this may also be a function of the faster ascent rates during Plinian eruptions at Colima, hindering the formation of significant reaction rims as seen in these rocks. Macías et al. (2017) reports the presence of 'Group 1' amphiboles with higher  $Al^{IV}$  and MgO contents, and interpret the origin of these amphiboles to be from magmas which triggered the Plinian event, compared to the resident Groups 2+3 amphiboles. All the amphiboles examined in this study were more akin to the Groups 2

and 3 amphiboles and not Group 1, suggesting they represent the amphiboles typically resident in the magmatic system. The most vesicular sample from the July 2015 event encountered in this study has a porosity of c. 40%, however the majority of the material has a much lower porosity, in contrast to the more porous scoria and pumice from Plinian eruptions. Although storage depths estimated from pyroxene thermobarometry are deeper than those from the literature, we see no significant difference in pre-eruptive storage between the July 2015 eruption and less intense effusive activity before and after, where we would expect to see the involvement of material from deeper in the plumbing system during an event more akin to a sub-Plinian or Plinian eruption. An abundance of reverse-zoned crystals, which would be expected following a large injection event from depth, is not seen here where reverse-zoned crystals are mostly rare and only make up a small percentage in some units after July 2015. Finally, the phase assemblage and proportions erupted in our samples from the 2015 event are consistent with the rest of the 2013-17 eruptive phase, and unlike those from 1913 or 1818.

We therefore conclude that the 2015 event, despite being intense, is unlikely to represent a cycle-ending eruption as proposed by Luhr (2002) and agree with the suggestion by Reyes-Dávila et al. (2016) that it may represent an 'end-member example of normal variation' involving the less degassed magmas already present in the system. We add that the appearance of reverse-zoned pyroxene crystals, reflecting mafic recharge followed by eruption, may nevertheless have had a role in the priming and potentially triggering the eruption of this already present magma.

## 7. CONCLUSIONS

The 2013-17 eruptive phase at Volcán de Colima was characterised by typical interplinian activity comprised of effusive lava flows, Vulcanian explosions, ashfall, PDCs and ballistic ejecta. The rocks erupted during this eruptive period were geochemically and mineralogically homogeneous andesites, similar to previous interplinian phases. A detailed study of the crystal cargo reveals a more complex picture of resident evolved melts injected by more mafic magmas within a mushy subvolcanic plumbing system:

1. Whole-rock compositions for andesites erupted during this period are relatively homogeneous and are comparable to the chemistry of rocks erupted during the 1998-2005 period of activity. Minor deviations in whole-rock Mg# and Cr content in ash samples from 2015-16 can be accounted for clinopyroxene+orthopyroxene accumulation rather than a genuine mafic trend. The compositions suggest that the magmatic system is buffered against

large changes in bulk composition despite evidence of mixing between evolved and mafic melts.

2. Pyroxenes with varied core compositions (Mg#~69-88) reflect crystallisation from melts within a heterogeneous magma mush. Whilst the bulk of the magma is relatively evolved, crystallising Mg# 69-75 pyroxene, the presence of resorption and disequilibrium textures, and high-Mg# and Cr<sub>2</sub>O<sub>3</sub> mafic bands and rims reflect periodic recharge of mafic melts and remobilisation of mush material. Evidence for mafic recharge is also seen in pervasive resorption of high An antecrystic plagioclase cores and surface resorption mantled by high An bands, and the presence of remobilised and reacting out olivine.
3. Mineral chemistry and petrography indicate at least two broad magmatic environments: an evolved end-member, crystallising Mg# 69-75 pyroxene, low An plagioclase, Fe-Ti oxides and apatite and possibly amphibole at between 980-1000°C ± 18°C, and a mafic magmatic end-member crystallising high-Mg# pyroxene, high An plagioclase, and olivine between 1020-1080°C ± 18°C. Pressure estimates typically vary between 4-6 kbar or c. 12-18 km depth.
4. These observations of a melt-rich mushy body in the mid-crust are consistent with geophysical evidence suggesting such a body at this depth. The storage conditions reported here are different from those proposed by melt inclusion studies, and more work must be done to constrain the nature of the body and pre-eruptive storage depths in the Volcán de Colima system.
5. Point counting of different crystal types reveal that most of the crystals (>60% phenocrysts, >90% micromicocrysts) are Homogeneous evolved type. Whilst reverse zoned crystals are rare or absent at the start of the eruptive phase, an increased frequency (up to 10% of all phenocrysts) of reverse zoned pyroxenes was recorded in lavas erupted after the intense VEI 3 eruption in July 2015. This suggests there may be a causal link between frequency of mafic injection and intensity of eruption, and further work, including estimating pre-eruptive storage timescales, should attempt to constrain this relationship.

As analytical workflows continue to accelerate, the prospect of petrological monitoring as a tool for actively monitoring volcanoes is becoming more achievable, rather than being restricted to a retrospective tool for understanding past eruptions. At Volcán de Colima, whole-rock compositions can provide valuable information such as greater mafic input leading up to eruptions (Luhr and Carmichael, 1990), however as we have discussed this may hide important information about magma dynamics. We demonstrate here that understanding the mineral populations can unlock more detailed information about magma dynamics in the plumbing system at Volcán de Colima, which could be incorporated into petrological monitoring schemes (e.g. relative proportion of

reverse-zoned crystals as evidence for increased mafic input). Magma mixing and storage depths in the mid-crust suggest that geophysical monitoring should also actively include this region as well as shallower depths. Finally, further work is needed to constrain the relationship between the frequency and volume of mafic recharge and evidence in the crystal record, the timescales of residence and mixing of these mafic magmas, and the relationships between recharge and monitoring data, before these crystal populations can be reliably used as a monitoring tool.

#### **CRedit Author Contribution Statement**

**Gerallt E. Hughes:** Writing – Original Draft, Methodology, Visualisation, Investigation. **Chiara Maria Petrone:** Conceptualisation, Supervision, Methodology, Writing – Review and Editing. **Hilary Downes:** Conceptualisation, Supervision, Writing – Review and Editing. **Cliff R. Varley:** Conceptualisation, Supervision, Resources, Writing – Review and Editing. **Samanta J. Hammond:** Resources, Writing – Review and Editing.

#### **Declaration of Competing Interest**

The authors declare that they have no known competing financial interests or personal relationships that could have appeared to influence the work reported in this paper.

#### **Acknowledgements**

This work was supported by the Natural Environment Research Council [grant number NE/L002485/1] to GEH. We would like to thank John Spratt, Alex Ball and Innes Clatworthy of the Image and Analysis Centre and Callum Hatch in the rock preparation lab at the NHM for their assistance in preparing and analysing thin sections. We would like to thank Katrina Kerr for their invaluable assistance in analysing the whole-rock compositional data and guidance in processing. We thank Etienne Médard and an anonymous reviewer for their kind words and in-depth review, and for making the manuscript more impactful. We would also like to thank Martin Mangler, Finley Gilchrist, Kate Laxton, Jack Anderson, and Barbara Kunz for our enlightening discussions during the project which lead to a much greater manuscript. We would like to thank the Faculty of Sciences at the University of Colima for logistical and material assistance during fieldwork, and for hosting GEH during fieldwork and sample collection. Finally, we are indebted to the many volunteers at CIIV who, over many years, have collected data and samples, and particularly those who provided invaluable field assistance during our fieldwork in 2018.

## **8. REFERENCES**

- Allan, J.F., 1986. Geology of the Northern Colima and Zacoalco Grabens, southwest Mexico: Late Cenozoic rifting in the Mexican volcanic belt. *Geological Society of America Bulletin* 97 (4), 473-485. [https://doi.org/10.1130/0016-7606\(1986\)97%3C473:GOTNCA%3E2.0.CO;2](https://doi.org/10.1130/0016-7606(1986)97%3C473:GOTNCA%3E2.0.CO;2)
- Allan, J.F., Carmichael, I.S.E., 1984. Lamprophyric lavas in the Colima graben, SW Mexico. *Contributions to Mineralogy and Petrology* 88, 203-216. <https://doi.org/10.1007/BF00380166>.
- Andersen, D.J., Lindsley, D.H., 1988. Internally consistent solution models for Fe-Mg-Mn-Fe-Ti oxides. *American Mineralogist* 73, 714-726.
- Andersen, D.J., Lindsley, D.H., Davidson, P.M., 1993. QUILF - a Pascal program to assess equilibria among Fe-Mg-Mn-Ti oxides, pyroxenes, olivine, and quartz. *Computers & Geosciences* 19 (9), 1333-1350. [https://doi.org/10.1016/0098-3004\(93\)90033-2](https://doi.org/10.1016/0098-3004(93)90033-2)
- Anderson, A.T., 1976. Magma mixing: Petrological process and volcanological tool. *Journal of Volcanology and Geothermal Research* 1, 3-33. [https://doi.org/10.1016/0377-0273\(76\)90016-0](https://doi.org/10.1016/0377-0273(76)90016-0)
- Arámbula-Mendoza, R., Reyes-Dávila, G., Vargas-Bracamontes, D.M., González-Amezcuca, M., Navarro-Ochoa, C., Martínez-Fierros, A., Ramírez-Vázquez, A., 2018. Seismic monitoring of effusive-explosive activity and large lava dome collapses during 2013–2015 at Volcán de Colima, Mexico. *Journal of Volcanology and Geothermal Research*, 351, 75-88. <https://doi.org/10.1016/j.jvolgeores.2017.12.011>
- Arámbula-Mendoza, R., Varley, N., García-Flores, R., Vargas-Bracamontes, D.M., Navarro-Ochoa, C., Márquez-Ramírez, V.H., Capra, L., González-Amezcuca, M., Martínez-Fierros, A., Ramírez-Vázquez, C.A., 2020. Destruction of a lava dome observed with photogrammetry, acoustic and seismic sensors at Volcán de Colima, Mexico. *Journal of Volcanology and Geothermal Research* 395, 106834. <https://doi.org/10.1016/j.jvolgeores.2020.106834>
- Atlas, Z.D., Dixon, J.E., Sen, G., Finny, M., Martin-Del Pozzo, A.L., 2006. Melt inclusions from Volcán Popocatepetl and Volcán de Colima, Mexico: Melt evolution due to vapor-saturated crystallization during ascent. *Journal of Volcanology and Geothermal Research*, 153 (3-4), 221–240. <https://doi.org/10.1016/j.jvolgeores.2005.06.010>
- Bachmann, O., Huber, C., 2016. Silicic magma reservoirs in the Earth's crust. *American Mineralogist* 101 (11), 2377-2404. <https://doi.org/10.2138/am-2016-5675>
- Bergantz, G.W., Schleicher, J.W., Burgisser, A., 2015. Open-system dynamics and mixing in magma mushes. *Nature Geoscience* 8, 793–796. <https://doi.org/10.1038/ngeo2534>
- Blundy, J., Cashman, K.V., 2003. Petrologic Reconstruction of Magmatic System Variables and Processes. *Reviews in Mineralogy and Geochemistry* 69 (1), 179–239. <https://doi.org/10.2138/rmg.2008.69.6>
- Breton-González, M.R., Ramírez, J.J., Navarro, C., 2002. Summary of the historical eruptive activity of Volcán De Colima, Mexico 1519-2000. *Journal of Volcanology and Geothermal Research*, 117 (1–2), 21–46. [https://doi.org/10.1016/S0377-0273\(02\)00233-0](https://doi.org/10.1016/S0377-0273(02)00233-0)
- Capra, L., Macías, J.L., Cortés, A., Dávila, N., Saucedo, R., Osorio-Ocampo, S., Arce, J.L., Gavilanes-Ruiz, J.C., Corona-Chávez, P., García-Sánchez, L., Sosa-Ceballos, G., Vázquez, R., 2016. Preliminary report on the July 10-11, 2015 eruption at Volcán de Colima: Pyroclastic density currents with exceptional runouts and volume. *Journal of Volcanology and Geothermal Research* 310, 39-49. <https://doi.org/10.1016/j.jvolgeores.2015.11.022>
- Carmichael, I.S.E., Frey, H.M., Lange, R.A., Hall, C.M., 2006. The Pleistocene cinder cones surrounding Volcán Colima, Mexico re-visited: eruption ages and volumes, oxidation states, and sulfur content. *Bulletin of Volcanology* 68, 407–419. <https://doi.org/10.1007/s00445-005-0015-8>
- Cashman, K.V., Giordano, G., 2014. Calderas and magma reservoirs. *Journal of Volcanology and Geothermal Research* 288, 28-45. <https://doi.org/10.1016/j.jvolgeores.2014.09.007>

- Cashman, K.V., Sparks, R.S.J., Blundy, J.D., 2017. Vertically extensive and unstable magmatic systems: A unified view of igneous processes. *Science* 355 (6331), eaag3055. <https://doi.org/10.1126/science.aag3055>
- Cassidy, M., Cole, P.D., Hicks, K.E., Varley, N.R., Peters, N., Lerner, A.H., 2015. Rapid and slow: Varying magma ascent rates as a mechanism for Vulcanian explosions. *Earth and Planetary Science Letters* 420, 73–84. <https://doi.org/10.1016/j.epsl.2015.03.025>
- Cassidy, M., Manga, M., Cashman, K., Bachmann, O., 2018. Controls on explosive-effusive volcanic eruption styles. *Nature Communications* 9, 2839. <https://doi.org/10.1038/s41467-018-05293-3>
- Conway, C.E., Chamberlain, K.J., Harigane, Y., Morgan, D.J., Wilson, C.J.N., 2020. Rapid assembly of high-Mg andesites and dacites by magma mixing at a continental arc stratovolcano. *Geology* 48 (10), 1033–1037. <https://doi.org/10.1130/G47614.1>
- Cooper, K.M., Kent, A.J.R., 2014. Rapid remobilization of magmatic crystals kept in cold storage. *Nature* 506, 480–483. <https://doi.org/10.1038/nature12991>
- Coote, A.C., Shane, P., 2016. Crystal origins and magmatic system beneath Ngauruhoe volcano (New Zealand) revealed by plagioclase textures and compositions. *Lithos* 260, 107–119. <https://doi.org/10.1016/j.lithos.2016.05.017>
- Cortés, A., Garduño, V.H., Macías, J.L., Navarro-Ochoa, C., Komorowski, J.C., Saucedo, R., Gavilanes, J.C., 2010. Geologic mapping of the Colima volcanic complex (Mexico) and implications for hazard assessment. In: Giampelli, G., Viereck-Goette, L. (Eds.) *Stratigraphy and Geology of Volcanic Areas: Geological Society of America Special Papers*. pp. 249–264. [https://doi.org/10.1130/2010.2464\(12\)](https://doi.org/10.1130/2010.2464(12))
- Cortés, A., Komorowski, J.-C., Macías, J.L., Capra, J., Mayer P.W., 2019. Late Pleistocene-Holocene Debris Avalanche Deposits from Volcán de Colima, Mexico. In: Varley, N., Connor, C., Komorowski, J.-C. (Eds.), 2019. *Volcán de Colima: Portrait of a Persistently Hazardous Volcano*. Berlin: Springer. 313 p. [https://doi.org/10.1007/978-3-642-25911-1\\_4](https://doi.org/10.1007/978-3-642-25911-1_4)
- Crummy, J.M., Savov, I.P., Navarro-Ochoa, C., Morgan, D.J., Wilson, M., 2014. High-K Mafic Plinian Eruptions of Volcán de Colima, Mexico. *Journal of Petrology* 55 (11), 2155–2191. <https://doi.org/10.1093/petrology/egu053>
- Davidson, J.P., Morgan, D.J., Charlier, B. L. A., Harlou, R., Hora, J. M., 2007. Microsampling and isotopic analysis of igneous rocks: implications for the study of magmatic systems. *Annual Review of Earth and Planetary Sciences* 35, 273–311. <https://doi.org/10.1146/annurev.earth.35.031306.140211>
- Edmonds M., Cashman K.V., Molness M., Jackson M., 2019. Architecture and dynamics of magma reservoirs. *Philosophical Transactions of the Royal Society A* 377 (2139):20180298, 1–29. <http://doi.org/10.1098/rsta.2018.0298>
- Eichelberger, J.C., Izbel'ov, P.E., Browne, B.L., 2006. Bulk chemical trends at arc volcanoes are not liquid lines of descent. *Lithos* 87 (1-2), 135–154. <https://doi.org/10.1016/j.lithos.2005.05.006>
- Erdmann, S., Martel, C., Pichavant, M., Kushnir, A., 2014. Amphibole as an archivist of magmatic crystallization conditions: problems, potential, and implications for inferring magma storage prior to the paroxysmal 2010 eruption of Mount Merapi, Indonesia. *Contributions to Mineralogy and Petrology* 167, 1016. <https://doi.org/10.1007/s00410-014-1016-4>
- Fabbro, G. N., Druitt, T. H., Costa, F., 2017. Storage and eruption of silicic magma across the transition from dominantly effusive to caldera-forming states at an arc volcano (Santorini, Greece). *Journal of Petrology* 58 (12), 2429–2464. <https://doi.org/10.1093/petrology/egy013>
- Ferrari, L. Orozco-Esquivel, T., Manea, V., Manea, M., 2012. The dynamic history of the Trans-Mexican Volcanic Belt and the Mexico subduction zone. *Tectonophysics* 522–523, 122–149. <https://doi.org/10.1016/j.tecto.2011.09.018>

- Gavilanes-Ruiz, J.C., Cuevas-Muñiz, A., Varley, N., Gwynne, G., Stevenson, J., Saucedo-Girón, R., Pérez-Pérez, A., Aboukhalil, M., Cortés-Cortés, A., 2009. Exploring the factors that influence the perception of risk: The case of Volcán de Colima, Mexico. *Journal of Volcanology and Geothermal Research* 186 (3-4), 238-252. <https://doi.org/10.1016/j.jvolgeores.2008.12.021>
- Ginibre, C., Wörner, G., Kronz, A., 2002. Minor- and trace-element zoning in plagioclase: implications for magma chamber processes at Paríacota volcano, northern Chile. *Contributions to Mineralogy and Petrology* 143, 300–315. <https://doi.org/10.1007/s00410-002-0351-z>
- Gómez-Tuena, A., Mori, L., Goldstein, S.L., Pérez-Arvizu, O., 2011. Magmatic diversity of western Mexico as a function of metamorphic transformations in the subducted oceanic plate. *Geochimica et Cosmochimica Acta* 75, 213-241. <https://doi.org/10.1016/j.gca.2010.09.029>
- Hawthorne, F.C., Oberti, R., Harlow, G.E., Maresch, W.V., Martín, R.F., Schumacher, J.C., Welch, M.D., 2012. Nomenclature of the amphibole supergroup. *American Mineralogist* 97 (11-12), 2031-2048. <https://doi.org/10.2138/am.2012.4276>
- Holness, M.B., Stock, M.J., Geist, D., 2019. Magma chambers versus mush zones: constraining the architecture of sub-volcanic plumbing systems from microstructural analysis of crystalline enclaves. *Philosophical Transactions of the Royal Society A* 377 (2139):20180006, 1-28. <https://doi.org/10.1098/rsta.2018.0006>
- Jochum, K.P., Nohl, U., Herwig, K., Lammel, E., Stoll, G., Hofmann, A.W., 2007. GeoReM: A New Geochemical Database for Reference Materials and Isotopic Standards. *Geostandards and Geoanalytical Research* 29 (3), 333-338. <https://doi.org/10.1111/j.1751-908X.2005.tb00904.x>
- Kent, A.J.R., 2008. Melt Inclusions in Basaltic and Related Volcanic Rocks. *Reviews in Mineralogy and Geochemistry* 69 (1), 273-352. <https://doi.org/10.2138/rmg.2008.69.8>
- Kilgour, G.N., Saunders, K.E., Blundy, J.D., Cashman, K.V., Scott, B. J., Miller, C.A., 2014. Timescales of magmatic processes at Ruapehu volcano from diffusion chronometry and their comparison to monitoring data. *Journal of Volcanology and Geothermal Research* 288, 62-75. <https://doi.org/10.1016/j.jvolgeores.2014.09.010>
- Kiser, E., Palomeras, I., Levanon, A., Zelt, C., Harder, S., Schmandt, B., Hansen, S., Creager, K., Ulberg, C., 2016. Magma reservoirs from the upper crust to the Moho inferred from high-resolution Vp and Vs models beneath Mount St. Helens, Washington State, USA. *Geology* 44 (6), 1111-1114. <https://doi.org/10.1130/G37591.1>
- Koleszar, A.M., Kent, A.J.R., Wallace, P.J., Scott, W.E., 2012. Controls on long-term low explosivity at andesitic arc volcanoes: Insights from Mount Hood, Oregon. *Journal of Volcanology and Geothermal Research* 219-220, 1-14. <https://doi.org/10.1016/j.jvolgeores.2012.01.003>
- Kozono, T., Koyaguchi, T., 2009. Effects of relative motion between gas and liquid on 1-dimensional steady flow in silicic volcanic conduits: 2. Origin of diversity of eruption styles. *Journal of Volcanology and Geothermal Research* 180 (1), 37-49. <https://doi.org/10.1016/j.jvolgeores.2008.11.007>
- Le Maitre, R. W., Bateman, P., Dudek, A., Keller, J., Lameyre, J., Le Bas, M. J., Sabine, P. A., Schmid, R., Sorensen, H., Streckeisen, A., Woolley, A. R., Zanettin, B., 1989. A Classification of Igneous Rocks and Glossary of Terms: Recommendations of the International Union of Geological Sciences Subcommission on the Systematics of Igneous Rocks. Oxford: Blackwell Scientific.
- Leake, B.E., Woolley, A.R., Arps, C.E.S., Birch, W.D., Gilbert, M.C., Grice, J.D., Hawthorne, F.C., Kato, A., Kisch, H.J., Krivovichev, V.G., Linthout, K., Laird, J., Mandarino, J.A., Maresch, W.V., Nickel, E.H., Rock, N.M.S., Schumacher, J.C., Smith, D.C., Stephenson, N.C.N., Ungaretti, L., Whittaker, E.J.W., Youzhi, G., 1997. Nomenclature of amphiboles: Report



- of the subcommittee on amphiboles of the international mineralogical association, commission on new minerals and mineral names. *The Canadian Mineralogist*, 35 (1), 219-246.
- Luhr, J.F., 1992. Slab-derived fluids and partial melting in subduction zones: insights from two contrasting Mexican volcanoes (Colima and Ceboruco). *Journal of Volcanology and Geothermal Research* 54 (1-2), 1-18. [https://doi.org/10.1016/0377-0273\(92\)90111-P](https://doi.org/10.1016/0377-0273(92)90111-P)
- Luhr, J.F., 1997. Extensional tectonics and the diverse primitive volcanic rocks in the western Mexican volcanic belt. *The Canadian Mineralogist*, 35 (2), 473-500.
- Luhr, J.F., 2002. Petrology and geochemistry of the 1991 and 1998-1999 lava flows from Volcán de Colima, México: Implications for the end of the current eruptive cycle. *Journal of Volcanology and Geothermal Research* 117 (1-2), 169-194. [https://doi.org/10.1016/S0377-0273\(02\)00243-3](https://doi.org/10.1016/S0377-0273(02)00243-3)
- Luhr J.F., 2006. The 1913 VEI-4 Plinian Eruption of Volcán de Colima (Mexico): tephrochronology, petrology, and plume modelling. *Eos, Transactions, American Geophysical Union*, 87 (52) (2006) Fall Meeting Supplement, Abstract V43B-1786.
- Luhr, J.F., Carmichael, I.S.E., 1980. The Colima volcanic complex, Mexico - I. Post-Caldera Andesites from Volcán Colima. *Contributions to Mineralogy and Petrology* 71 (4), 343-372. <https://doi.org/10.1007/BF00374707>
- Luhr, J.F., Carmichael, I.S.E., 1981. The Colima volcanic complex, Mexico: Part II. Late-quaternary cinder cones. *Contributions to Mineralogy and Petrology* 76, 127-147. <https://doi.org/10.1007/BF00371954>
- Luhr, J.F., Carmichael, I.S.E., 1982. The Colima Volcanic Complex, Mexico: III. Ash- and Scoria-Fall Deposits from the Upper Slopes of Volcán Colima. *Contributions to Mineralogy and Petrology* 80, 262-275. <https://doi.org/10.1007/BF00371356>
- Luhr, J.F., Carmichael, I.S.E., 1990. Petrological monitoring of cyclical eruptive activity at Volcán Colima, Mexico. *Journal of Volcanology and Geothermal Research* 42 (3), 235-260. [https://doi.org/10.1016/0377-0273\(90\)90002-W](https://doi.org/10.1016/0377-0273(90)90002-W)
- Luhr, J.F., Prestegard, K.L., 1988. Caldera formation at Volcán Colima, Mexico, by a large Holocene volcanic debris avalanche. *Journal of Volcanology and Geothermal Research* 35 (4), 335-348. [https://doi.org/10.1016/0377-0273\(88\)90027-3](https://doi.org/10.1016/0377-0273(88)90027-3)
- Luhr, J.F., Navarro-Ochoa, C., Savov, I.P., 2010. Tephrochronology, petrology and geochemistry of Late-Holocene pyroclastic deposits from Volcán de Colima, Mexico. *Journal of Volcanology and Geothermal Research* 197 (1-4), 1-32. <https://doi.org/10.1016/j.jvolgeores.2009.11.007>
- Macías, J.L., Sosa-Ceballos G., Arce, J.L., Gardner, J.E., Saucedo, R., Valdez-Moreno, G., 2017. Storage conditions and magma processes triggering the 1818 CE Plinian eruption of Volcán de Colima. *Journal of Volcanology and Geothermal Research* 340, 117-129. <https://doi.org/10.1016/j.jvolgeores.2017.02.025>.
- Macorps, E., Charbonnier, S.J., Varley, N.R., Capra, L., Atlas, Z. and Cabré, J., 2018. Stratigraphy, sedimentology and inferred flow dynamics from the July 2015 block-and-ash flow deposits at Volcán de Colima, Mexico. *Journal of Volcanology and Geothermal Research* 349, 99-116. <https://doi.org/10.1016/j.jvolgeores.2017.09.025>
- Mangler, M.F., Prytulak, J., Gisbert, G., Delgado-Granados, H., Petrone, C. M., 2019. Interplinian effusive activity at Popocatepetl volcano, Mexico: New insights into evolution and dynamics of the plumbing system. *Volcanica* 2 (1), 45-72. <https://doi.org/10.30909/vol.02.01.4572>
- Mangler, M.F., Petrone, C.M., Hill, S., Delgado-Granados, H., Prytulak, J., 2020. A Pyroxenic View on Magma Hybridization and Crystallization at Popocatepetl Volcano, Mexico. *Frontiers in Earth Science* 8:362, 1-22. <https://doi.org/10.3389/feart.2020.00362>

- Martin-Del Pozzo, A.L., Rodríguez, A., Portocarrero, J., 2016. Reconstructing 800 years of historical eruptive activity at Popocatepetl Volcano, Mexico. *Bulletin of Volcanology* 78:18, 1-13. <https://doi.org/10.1007/s00445-016-1010-y>
- Moorbath, S., Thorpe, R.S., Gibson, I.L., 1978. Strontium isotope evidence for petrogenesis of Mexican andesites. *Nature* 271, 437-439. <https://doi.org/10.1038/271437a0>
- Moore, G., Carmichael, I. S. E., 1998. The hydrous phase equilibria (to 3 kbar) of an andesite and basaltic andesite from western Mexico: constraints on water content and conditions of phenocryst growth. *Contributions to Mineralogy and Petrology* 130, 304-319. <https://doi.org/10.1007/s004100050367>
- Mora, J.C., Macías, J.L., Saucedo, R., Orlando, A., Manetti, P., Vaselli, O., 2002. Petrology of the 1998-2000 products of Volcán de Colima, México. *Journal of Volcanology and Geothermal Research* 117 (1-2), 195–212. [https://doi.org/10.1016/S0377-0273\(02\)00244-5](https://doi.org/10.1016/S0377-0273(02)00244-5)
- Murphy, M.D., Sparks, R.S.J., Barclay, J., Carroll, M.R., Brewer, T.S., 2000. Remobilization of Andesite Magma by Intrusion of Mafic Magma at the Soufrière Hills Volcano, Montserrat, West Indies. *Journal of Petrology* 41 (1), 21-42. <https://doi.org/10.1093/petrology/41.1.21>
- Neave, D.A., Putirka, K.D., 2017. A new clinopyroxene-liquid barometer, and implications for magma storage pressures under Icelandic rift zones. *American Mineralogist* 102 (4), 777-794. <https://doi.org/10.2138/am-2017-5968>
- Norini, G., Capra, L., Groppelli, G., Agliardi, F., Pola, A., Cortés, A., 2010. Structural architecture of the Colima Volcanic Complex. *Journal of Geophysical Research: Solid Earth*, 115:B12209, 1-20. <https://doi.org/10.1029/2010JB007649>
- Newhall, C.G., Self, S., 1982. The volcanic explosivity index (VEI): an estimate of explosive magnitude for historical volcanism. *Journal of Geophysical Research: Oceans and Atmospheres* 87 (C2), 1231-1238. <https://doi.org/10.1029/JC087iC02p01231>
- Norrish, K., Hutton, J.T., 1969. An accurate X-ray spectrographic method for the analysis of a wide range of geological samples. *Geochimica et Cosmochimica Acta*, 33 (4), 431-453. [https://doi.org/10.1016/0016-7037\(69\)90126-4](https://doi.org/10.1016/0016-7037(69)90126-4)
- Núñez-Cornú, F., Nava, A., De La Cruz Reyna, S., Jiménez, Z., Valencia, C., García-Arthur, R., 1994. Seismic activity related to the 1991 eruption of Colima Volcano, Mexico. *Bulletin of Volcanology* 56, 228–237. <https://doi.org/10.1007/BF00279608>
- Peccerillo A., Taylor S.R., 1970. Geochemistry of Eocene calcalkaline rocks from Kastamonu area northern Turkey. *Contributions to Mineralogy and Petrology* 68, 63-81. <https://doi.org/10.1007/BF00384745>
- Petrone, C.M., Orozco Esquivel, T., Ferrari, L., 2014. Petrogenesis and geodynamic significance of silicic volcanism in the western Trans-Mexican Volcanic Belt: role of gabbroic cumulates. *Contributions to Mineralogy and Petrology* 167:1006, 1-21. <https://doi.org/10.1007/s00410-014-1006-6>
- Petrone, C.M., Braschi, E., Francalanci, L., Casalini, M., Tommasini, S., 2018. Rapid mixing and short storage timescale in the magma dynamics of a steady-state volcano. *Earth and Planetary Science Letters* 492, 206–221. <https://doi.org/10.1016/j.epsl.2018.03.055>
- Petrosino, S., Cusano, P., La Rocca, M., Galluzzo, D., Orozco-Rojas, J., Bretón, M., Ibáñez, J., Del Pezzo, E., 2011. Source location of long period seismicity at Volcán de Colima, México. *Bulletin of Volcanology* 73, 887-898. <https://doi.org/10.1007/s00445-011-0447-2>
- Piccoli, P., Candela, P., 1994. Apatite in felsic rocks: a model for the estimation of initial halogen concentrations in the Bishop Tuff (Long Valley) and Tuolumne Intrusive Suite (Sierra Nevada Batholith) magmas. *American Journal of Science* 294 (1), 92–135. <https://doi.org/10.2475/ajs.294.1.92>
- Paulatto, M., Moorkamp, M., Hautmann, S., Hooft, E., Morgan, J.V., Sparks, R.S.J., 2019. Vertically Extensive Magma Reservoir Revealed From Joint Inversion and Quantitative

- Interpretation of Seismic and Gravity Data. *Journal of Geophysical Research: Solid Earth*, 124 (11), 11170-11191. <https://doi.org/10.1029/2019JB018476>
- Popa, R.-G., Bachmann, O., Ellis, B.S., Degruyter, W., Tollan, P., Kyriakopoulos, K., 2019. A connection between magma chamber processes and eruptive styles revealed at Nisyros-Yali volcano (Greece). *Journal of Volcanology and Geothermal Research*, 106666. <https://doi.org/10.1016/j.jvolgeores.2019.106666>
- Popa, R.-G., Dietrich, V.J., Bachmann, O., 2020. Effusive-explosive transitions of water-undersaturated magmas. The case study of Methana Volcano, South Aegean Arc. *Journal of Volcanology and Geothermal Research* 399, 106884. <https://doi.org/10.1016/j.jvolgeores.2020.106884>
- Putirka, K.D., 2008. Thermometers and Barometers for Volcanic Systems. *Reviews in Mineralogy and Geochemistry*, 69 (1), 61–120. <https://doi.org/10.2138/rmg.2008.69.3>
- Reubi, O., Blundy, J., 2008. Assimilation of plutonic roots, formation of High-K 'exotic' melt inclusions and genesis of andesitic magmas at Volcán de Colima, Mexico. *Journal of Petrology*, 49 (12), 2221–2243. <https://doi.org/10.1093/petrology/egn066>
- Reubi, O., Blundy, J., Varley, N.R., 2013. Volatiles content, degassing and crystallisation of intermediate magmas at Volcan de Colima, Mexico, inferred from melt inclusions. *Contributions to Mineralogy and Petrology* 165, 1087-1106. <https://doi.org/10.1007/s00410-013-0849-6>
- Reubi, O., Sims, K.W.W., Varley, N., Reagan, M., Eiker, J., 2015. Timescales of degassing and conduit dynamics inferred from  $^{210}\text{Pb}$ – $^{226}\text{Ra}$  disequilibria in Volcán de Colima 1998–2010 andesitic magmas. *Geological Society of London Special Publications*, 422, 189–206. <https://doi.org/10.1144/SP422.5>
- Reubi, O., Scott, S.R., Sims, K.W.W., 2017. Evidence of Young Crystal Ages in Andesitic Magmas from a Hyperactive Arc Volcano Volcan de Colima, Mexico. *Journal of Petrology* 58 (2), 261–276. <https://doi.org/10.1093/petrology/egx015>
- Reubi, O., Blundy, J., Pickles, J., 2019. Petrological Monitoring of Volcan de Colima Magmatic System: The 1998 to 2011 Activity. In: Varley, N., Connor, C., Komorowski, J.-C. (Eds.), 2019. *Volcán de Colima: Portrait of a Persistently Hazardous Volcano*. Berlin: Springer. pp. 219-240. [https://doi.org/10.1007/978-3-642-25911-1\\_9](https://doi.org/10.1007/978-3-642-25911-1_9)
- Reyes-Dávila, G.A., Arámbula-Mendoza, R., Espinasa-Pereña, R., Pankhurst, M.J., Navarro-Ochoa, C., Savov, I., Vargas Bracamontes, D.M., Cortés-Cortés, A., Gutiérrez-Martínez, C., Valdés-González, C., Domínguez-Reyes, T., González-Amezcuca, M., Martínez-Fierros, A., Ramírez-Vázquez, C.A., Cárdenas-González, L., Castañeda-Bastida, E., Vázquez Espinoza de los Montes, D.M., Nieto-Torres, A., Campion, R., Courtois, L., Lee, P.D., 2016. Volcán de Colima dome collapse of July, 2015 and associated pyroclastic density currents. *Journal of Volcanology and Geothermal Research* 320, 100-106. <https://doi.org/10.1016/j.jvolgeores.2016.04.015>
- Ridolfi, F., Renzulli, A., Puerini, M., 2010. Stability and chemical equilibrium of amphibole in calc-alkaline magmas: An overview, new thermobarometric formulations and application to subduction-related volcanoes. *Contributions to Mineralogy and Petrology* 160, 45-66. <https://doi.org/10.1007/s00410-009-0465-7>
- Robin, C., Mossand, P., Camus, G., Cantagrel, J.M., Gourgaud, A., Vincent, P.M., 1987. Eruptive history of the Colima volcanic complex (Mexico). *Journal of Volcanology and Geothermal Research* 31 (1–2), 99–113. [https://doi.org/10.1016/0377-0273\(87\)90008-4](https://doi.org/10.1016/0377-0273(87)90008-4)
- Robin, C., Komorowski, J.C., Boudal, C., Mossand, P., 1990. Mixed-magma pyroclastic surge deposits associated with debris avalanche deposits at Colima volcanoes, Mexico. *Bulletin of Volcanology* 52, 391–403. <https://doi.org/10.1007/BF00302051>
- Robin, C., Camus, G., Gourgaud, A., 1991. Eruptive and magmatic cycles at Fuego de Colima volcano (Mexico). *Journal of Volcanology and Geothermal Research* 45 (3-4), 209-225. [https://doi.org/10.1016/0377-0273\(91\)90060-D](https://doi.org/10.1016/0377-0273(91)90060-D)

- Ruprecht, P., Bachmann, O., 2010. Pre-eruptive reheating during magma mixing at Quizapu volcano and the implications for the explosiveness of silicic arc volcanoes. *Geology* 38 (10), 919-922. <https://doi.org/10.1130/G31110.1>
- Ruprecht, P., Plank, T., 2013. Feeding andesitic eruptions with a high-speed connection from the mantle. *Nature* 500, 68-72. <https://doi.org/10.1038/nature12342>
- Rutherford, M.J., Devine, J.D., 2003. Magmatic Conditions and Magma Ascent as Indicated by Hornblende Phase Equilibria and Reactions in the 1995–2002 Soufrière Hills Magma. *Journal of Petrology* 44 (8), 1433–1453. <https://doi.org/10.1093/petrology/44.8.1433>
- Rutherford, M.J., Hill, P.M., 1993. Magma ascent rates from amphibole breakdown: An experimental study applied to the 1980–1986 Mount St. Helens eruptions. *Journal of Geophysical Research*, 98 (B11), 19667–19685. <https://doi.org/10.1029/93JB01613>
- Saucedo, R., Macías, J.L., Sheridan, M.F., Bursik, M.I., Komorowski, J.-C., 2005. Modeling of pyroclastic flows of Colima Volcano, Mexico: Implications for hazard assessment. *Journal of Volcanology and Geothermal Research*, 139 (1–2), 103–115. <https://doi.org/10.1016/j.jvolgeores.2004.06.019>
- Saucedo, R., Macías, J.L., Gavilanes, J.C., Arce, J.L., Komorowski, J.-C., Gardner, J.E., Valdez-Moreno, G., 2010. Eyewitness, stratigraphy, chemistry, and eruptive dynamics of the 1913 Plinian eruption of Volcan de Colima, Mexico. *Journal of Volcanology and Geothermal Research* 191 (3–4), 149–166. <https://doi.org/10.1016/j.jvolgeores.2010.01.011>
- Savov, I.P., Luhr, J.F., Navarro-Ochoa, C., 2008. Petrology and geochemistry of lava and ash erupted from Volcán Colima, Mexico, during 1998-2005. *Journal of Volcanology and Geothermal Research* 174 (4), 241–256. <https://doi.org/10.1016/j.jvolgeores.2008.02.007>
- Schaaf, P., Carrasco-Núñez, G., 2010. Geochemical and isotopic profile of Pico de Orizaba (Citlaltépetl) volcano, Mexico: Insights for magma generation processes. *Journal of Volcanology and Geothermal Research* 197 (1–4), 108-122. <https://doi.org/10.1016/j.jvolgeores.2010.02.016>
- Scott, J.A.J., Mather, T.A., Pyle, D.M., Rose, W.I., Chigna, G., 2012. The magmatic plumbing system beneath Santiaguito Volcano, Guatemala. *Journal of Volcanology and Geothermal Research* 227-238, 54-68. <https://doi.org/10.1016/j.jvolgeores.2012.05.014>
- Shane, P., Cocker, K., Coote, A., Stirling, C.H., Reid, M.R., 2019. The prevalence of plagioclase antecrysts and xenocrysts in andesite magma, exemplified by lavas of the Tongariro volcanic complex, New Zealand. *Contributions to Mineralogy and Petrology* 174:89, 1-18. <https://doi.org/10.1007/s00410-019-1626-y>
- Sieron, K., Siebe, C., 2008. Revised stratigraphy and eruption rates of Ceboruco stratovolcano and surrounding monogenetic vents (Nayarit, Mexico) from historical documents and new radiocarbon dates. *Journal of Volcanology and Geothermal Research* 176 (2), 241-264. <https://doi.org/10.1016/j.jvolgeores.2008.04.006>
- Sparks, S. R. J., Sigurdsson, H., Wilson, L., 1977. Magma mixing: A mechanism for triggering acid explosive eruptions. *Nature* 267, 315–318. <https://doi.org/10.1038/267315a0>
- Spica, Z., Pertou, M., Legrand, D., 2017. Anatomy of the Colima volcano magmatic system, Mexico. *Earth and Planetary Science Letters* 459, 1-13. <https://doi.org/10.1016/j.epsl.2016.11.010>
- Streck, M.J., 2008. Mineral Textures and Zoning as Evidence for Open System Processes. *Reviews in Mineralogy and Geochemistry* 69 (1), 595–622. <https://doi.org/10.2138/rmg.2008.69.15>
- Sychev, I.V., Koulakov, I., Egorushkin, I., Zhuravlev, S., West, M., El Khrepy, S., Al-Arifi, N., Alajmi, M.S., 2019. Fault-Associated Magma Conduits Beneath Volcán de Colima Revealed by Seismic Velocity and Attenuation Tomography Studies. *Journal of Geophysical Research: Solid Earth* 124 (8), 8908-8923. <https://doi.org/10.1029/2019JB017449>

- Varley, N.R., 2019. Monitoring the Recent Activity: Understanding a Complex System. In: Varley, N.R., Connor, C., Komorowski, J.-C. (Eds.), 2019. *Volcán de Colima: Portrait of a Persistently Hazardous Volcano*. Berlin: Springer. pp. 159-193  
[https://doi.org/10.1007/978-3-642-25911-1\\_12](https://doi.org/10.1007/978-3-642-25911-1_12)
- Verma, S.P., Luhr, J.F., 2010. Sr, Nd, and Pb isotopic evidence for the origin and evolution of the Cántaro-Colima volcanic chain, Western Mexican Volcanic Belt. *Journal of Volcanology and Geothermal Research* 197 (1-4), 33-51.  
<https://doi.org/10.1016/j.jvolgeores.2010.08.019>
- Waitz, P. 1915. Der Gegenwärtige Zustand der Mexikanischen Vulkane und die Letzte Eruption des Vulkans von Colima (1913). *Zeitschrift für Vulkanologie* 1, 247.
- Wallace, P.J., Carmichael, I.S.E., 1999. Quaternary volcanism near the Valley of Mexico: implications for subduction zone magmatism and the effects of crustal thickness variations on primitive magma compositions. *Contributions to Mineralogy and Petrology* 135, 291–314. <https://doi.org/10.1007/s004100050513>
- Wallace, P.A., Lamb, O.D., De Angelis, S., Kendrick, J.E., Hornby, A.L., Díaz-Moreno, A., González, P.J., von Aulock, F.W., Lamur, A., Utley, J.E.P., Rietbrock, A., Chigna, G., Lavallée, Y., 2020. Integrated constraints on explosive eruption intensification at Santiaguito dome complex, Guatemala. *Earth and Planetary Science Letters* 536:116139, 1-16  
<https://doi.org/10.1016/j.epsl.2020.116139>.
- Wanke, M., Karakas, O., Bachmann, O., 2019. The genesis of arc dacites: the case of Mount St. Helens, WA. *Contributions to Mineralogy and Petrology* 174:7  
<https://doi.org/10.1007/s00410-018-1547-6>
- Wells, P.R.A., 1977. Pyroxene thermometry in simple and complex systems. *Contributions to Mineralogy and Petrology* 62, 129-131. <https://doi.org/10.1007/BF00372872>
- Zobin, V.M., Luhr, J.F., Taran, Y.A., Bretton, M., Cortés, A., De La Cruz-Reyna, S., Domínguez, T., Galindo, I., Gavilanes, J.C., Muñoz, J.J., Navarro, C., Ramírez, J.J., Reyes, G.A., Ursúa, M., Velasco, J., Alatorre, E., Santiago, H., 2002. Overview of the 1997–2000 activity of Volcán de Colima, Mexico. *Journal of Volcanology and Geothermal Research* 117 (1–2), 1–19.  
[https://doi.org/10.1016/S3773-0273\(02\)00232-9](https://doi.org/10.1016/S3773-0273(02)00232-9)

### Figure Captions

**Figure 1. Location maps of Volcán de Colima** showing **A)** Volcán de Colima within Mexico (inset) and location of the volcano and roads (red lines) and settlements (grey). Road and settlements data from INEGI and digital elevation mode shaded relief base map from NASA SRTM; **B)** 2013-17 lava and pyroclastic flow deposits around the edifice. The collapse scar from previous edifice collapses is clearly seen as a scarp along the northern part of El Playón (red solid line), and is inferred from satellite imagery and digital elevation models in the south (red dashed line). The 2015 PDC extends c. 10 km to the south from the bottom of the map.

**Figure 2.** Summary of activity during the 2013-17 period of activity at Volcán de Colima, split into 5 phases for the purposes of this study according to the broad activity at the volcano. Light grey shading in ‘Slow dome growth and explosions’ indicate periods where the dome is no longer increasing in volume (e.g. during lava flows from the crater) or periods of very slow growth but with small explosions. Line extending from Phase 6 refers to continuing seismic activity and fumarolic

activity following the cessation of eruptive activity. Information from the Smithsonian's Global Volcanism Project (GVP), Varley (2019), Arámbula-Mendoza et al., 2020, and references in the text.

**Figure 3.** Chemical classification of Volcán de Colima andesites. A) Chemical classification according to scheme of Le Maitre et al. (1989), showing that the majority of samples are andesites. B) All studied samples plotted according to the  $K_2O$  v  $SiO_2$  classification scheme for calc-alkaline rocks (Peccerillo and Taylor, 1976; Le Maitre et al., 1989), and demonstrates that samples are medium-K andesites and overlap with typical Colima compositions. Symbol colours represent the phases of the 2013-17 eruption as shown in Figure 3. Light grey field represents historical Colima samples obtained from the GeoROC database (Luhr, 1992, 1997, 2002; Luhr and Carmichael, 1980, 1990; Luhr and Prestegard, 1988; Luhr et al., 2010; Moorbath et al., 1978; Mora et al., 2002; Reubi and Blundy, 2008; Reubi et al., 2017; Robin et al, 1987, 1991; Saucedo et al., 2010; Savov et al., 2008; Verma and Luhr, 2010).

**Figure 4.** Selected major and trace element plots of whole-rock compositions for Volcán de Colima andesites erupted the 2013-17 eruption, plotted against an index of differentiation (Mg-number). Symbolology as in Figure 3. Red shaded areas indicate liquid Mg# ranges which would crystallise equilibrium pyroxenes in the mafic (M) and evolved (E) end members. Equilibrium Mg# ranges for E extend to the left of the axis extents in these plots, and ranges for M extend off to the right of the axis extents.

**Figure 5.** Time series of selected sample compositions showing  $SiO_2$ , Mg# and Cr versus time. With the exception of minor deviations (see Section 5.1), most of the time series shows a relatively homogeneous bulk composition of these magmas. Analytical error for all three plots is smaller than the individual points. Blue solid (average) and grey dashed (minima and maxima) lines represent the range of compositions from the post-1913 (1961 to 2005) samples erupted at Volcan de Colima, using data obtained from the GeoROC database (Luhr, 1992, 1997, 2002; Luhr and Carmichael, 1980, 1990; Luhr and Prestegard, 1988; Luhr et al., 2010; Moorbath et al., 1978; Mora et al., 2002; Reubi and Blundy, 2008; Reubi et al., 2017; Robin et al, 1987, 1991; Saucedo et al., 2010; Savov et al., 2008; Verma and Luhr, 2010).

**Figure 6.** Pyroxene phenocryst types described in Volcán de Colima samples from the 2013-17 eruption. **A)** Typical low-Mg# homogeneous microphenocryst, with small apatite inclusions near the rim. **B)** Typical pyroxene assemblage within a glomerocryst. The agglomeration contains Normal Zoned, mostly Type 3 crystals, along with remnant olivine, plagioclase, oxides and interstitial melt. **C)** Typical Normal Zoned Type 1 phenocryst with rounded, low-Mg# core mantled by high-Mg# band

and low-Mg# rim. **D)** Normal Zoned Type 2 crystal with a rounded core of intermediate composition mantled by high-Mg# band and low-Mg# rim. The reverse-zoned crystals have a similar categorisation, but with the presence of a high-Mg# rim. **E)** Normal Zoned Type 3 crystal with a high-Mg# core rimmed by a low-Mg# rim. **F)** Type 1 Reverse-Zoned crystal with a low-Mg# core rimmed by high-Mg# rim, with sharp core-rim boundary.

**Figure 7.** Mg# distributions for the major normal and reverse zoned pyroxene phenocryst types, split according to subtype. Box plots show the average (black horizontal bar) and 1 standard deviation distributions at the top and bottom of the box. Pink field shows the typical range of Mg# for Homogeneous-type crystals.

**Figure 8.** Cr<sub>2</sub>O<sub>3</sub> versus Mg# plots for the major normal and reverse zoned pyroxene phenocryst types, split according to subtype. Normal zoned subtypes have a characteristic high-Mg or intermediate-Mg band marked simply as 'Band' for these plots. Due to the presence of evolved and mafic bands for the reverse-zoned types, these are differentiated using different symbols. In most cases, higher zone Mg-number is also associated with higher chromium content.

**Figure 9.** Modelled temperature estimates using the two-pyroxene geothermobarometer of Putirka (2008), grouped by crystal zone. Box represents the mean of temperature estimate values and bar represents 1 standard deviation. Colours as per the legend in Fig. 8.

**Figure 10.** Modelled temperature estimates using the two-pyroxene geothermobarometer of Putirka (2008), grouped by Mg#. Box represents the mean of temperature estimate values and bar represents 1 standard deviation. Point colours as per the legend in Fig. 8.

**Figure 11.** Modelled pressure estimates using the two-pyroxene geothermobarometer of Putirka (2008), grouped by crystal zone. Box represents the mean of pressure estimate values and bar represents 1 standard deviation. Colours as per the legend in Fig. 8.

**Figure 12.** Schematic model of the interactions between resident evolved melts and injections of mafic melts from depth in the plumbing system of Volcán de Colima.

**Figure 13.** Petrological model of the plumbing system at Volcán de Colima, combining petrological information from the findings of this study and published literature, along with geophysical evidence. General abbreviations include px (pyroxene), plag (plagioclase), ol (olivine), EQ (earthquake), DADs (Debris Avalanche Deposits). 'Gp II' refer to Plinian events with an alkalic component as described by Crummy et al. (2014).  $\delta$ -ve dVp refer to relative negative dVp values, and  $\delta$ +ve dVs refer to relative

positive dVs values, and used as evidence for silicic magmas in this part of the crust by Sychev et al. (2019). References as in the text.

Journal Pre-proof



**CRedit Author Contribution Statement**

**Gerallt E. Hughes:** Writing – Original Draft, Methodology, Visualisation, Investigation.

**Chiara Maria Petrone:** Conceptualisation, Supervision, Methodology, Writing – Review and Editing.

**Hilary Downes:** Conceptualisation, Supervision, Writing – Review and Editing.

**Nick R. Varley:** Conceptualisation, Supervision, Resources, Writing – Review and Editing.

**Samantha J. Hammond:** Resources, Writing – Review and Editing.

Journal Pre-proof

**Declaration of interests**

The authors declare that they have no known competing financial interests or personal relationships that could have appeared to influence the work reported in this paper.

The authors declare the following financial interests/personal relationships which may be considered as potential competing interests:

Journal Pre-proof

**Highlights**

- New petrological and geochemical data for the 2013-17 eruption at Volcán de Colima.
- Uniform paragenesis and geochemistry indicate efficient homogenisation of magmas.
- Injections of mafic melts into evolved reservoirs remobilise crystal mush material.
- Suggests mushy magmatic system in the mid-crust, agreeing with geophysical data.
- Mafic injections may have been related to the intense July 2015 eruption.

Journal Pre-proof

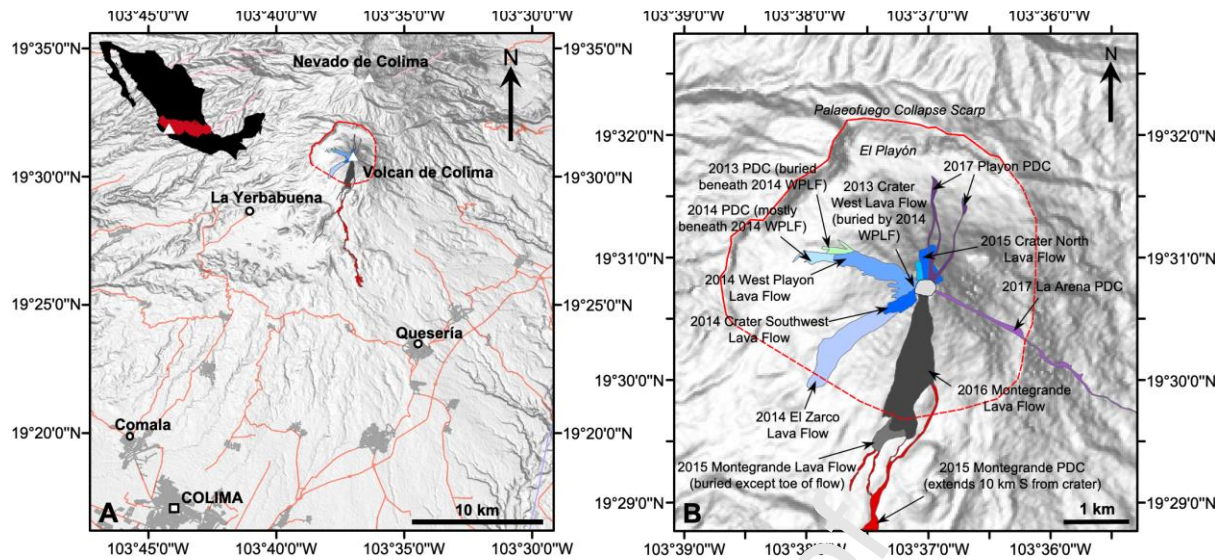


**Figure 1. Location maps of Volcán de Colima showing A) Volcán de Colima within Mexico (inset) and location of the volcano and roads (red lines) and settlements (grey). Road and settlements data from INEGI and digital elevation mode shaded relief base map from NASA SRTM; B) 2013-17 lava and pyroclastic flow deposits around the edifice. The collapse scar from previous edifice collapses is clearly seen as a scarp along the northern part of El Playón (red solid line), and is inferred from satellite imagery and digital elevation mode in the south (red dashed line). The 2015 PDC extends c. 10 km to the south from the bottom of the map.**

*[Full page width, 2-column, full colour]*

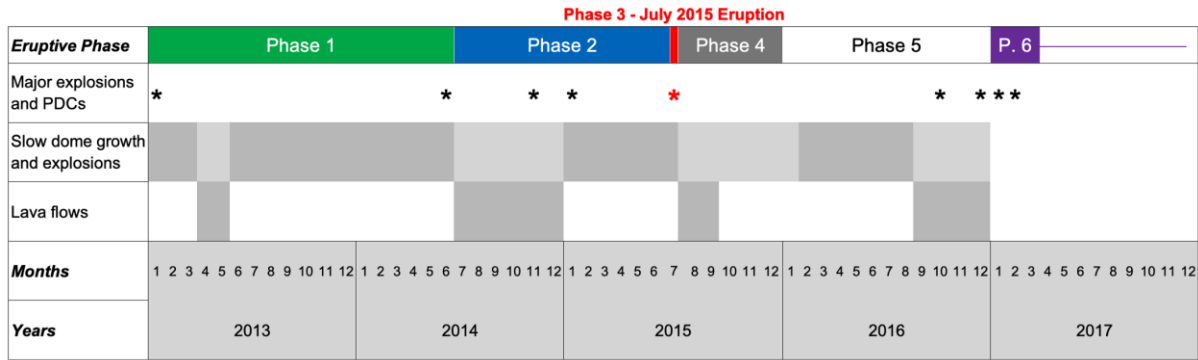


**Figure 2.** Summary of activity during the 2013-17 period of activity at Volcán de Colima, split into 5 phases for the purposes of this study according to the broad activity at the volcano. Light grey shading in ‘Slow dome growth and explosions’ indicate periods where the dome is no longer increasing in volume (e.g. during lava flows from the crater) or periods of very slow growth but with small explosions. Line extending from Phase 6 refers to continuing seismic activity and fumarolic activity following the cessation of eruptive activity. Information from the Smithsonian’s Global Volcanism Project (GVP), Varley (2019), Arámbula-Mendoza et al., 2020, and references in the text. *[Full page width, 2-column, full colour]*

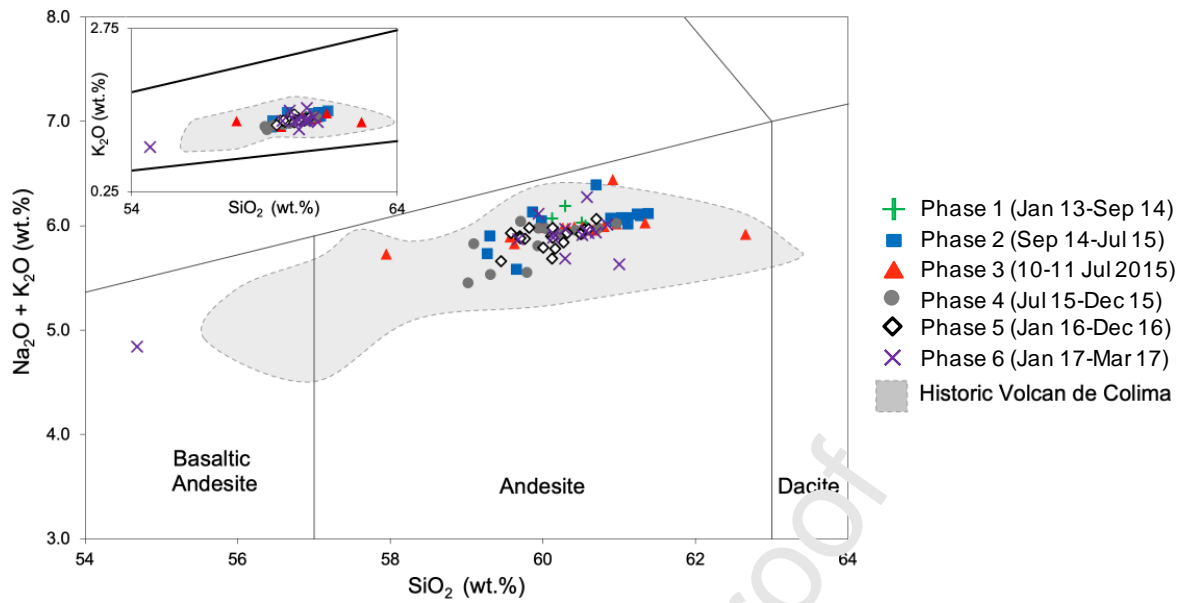


**Figure 3.** Chemical classification of Volcán de Colima andesites. A) Chemical classification according to scheme of Le Maitre et al. (1989), showing that the majority of samples are andesites. B) All studied samples plotted according to the  $\text{K}_2\text{O} - \text{SiO}_2$  classification scheme for calc-alkaline rocks (Peccerillo and Taylor, 1976; Le Maitre et al., 1989), and demonstrates that samples are medium-K andesites and overlap with typical Colima compositions. Symbol colours represent the phases of the 2013-17 eruption as shown in Figure 3. Light grey field represents historical Colima samples obtained from the GeoROC database (Luhr, 1992, 1997, 2002; Luhr and Carmichael, 1980, 1990; Luhr and Prestegard, 1988; Luhr et al., 2010; Moorbath et al., 1978; Mora et al., 2002; Reubi and Blundy, 2008; Reubi et al., 2017; Robin et al., 1987, 1991; Saucedo et al., 2010; Savov et al., 2008; Verma and Luhr, 2010).

[Full page width, 2-column, full colour]

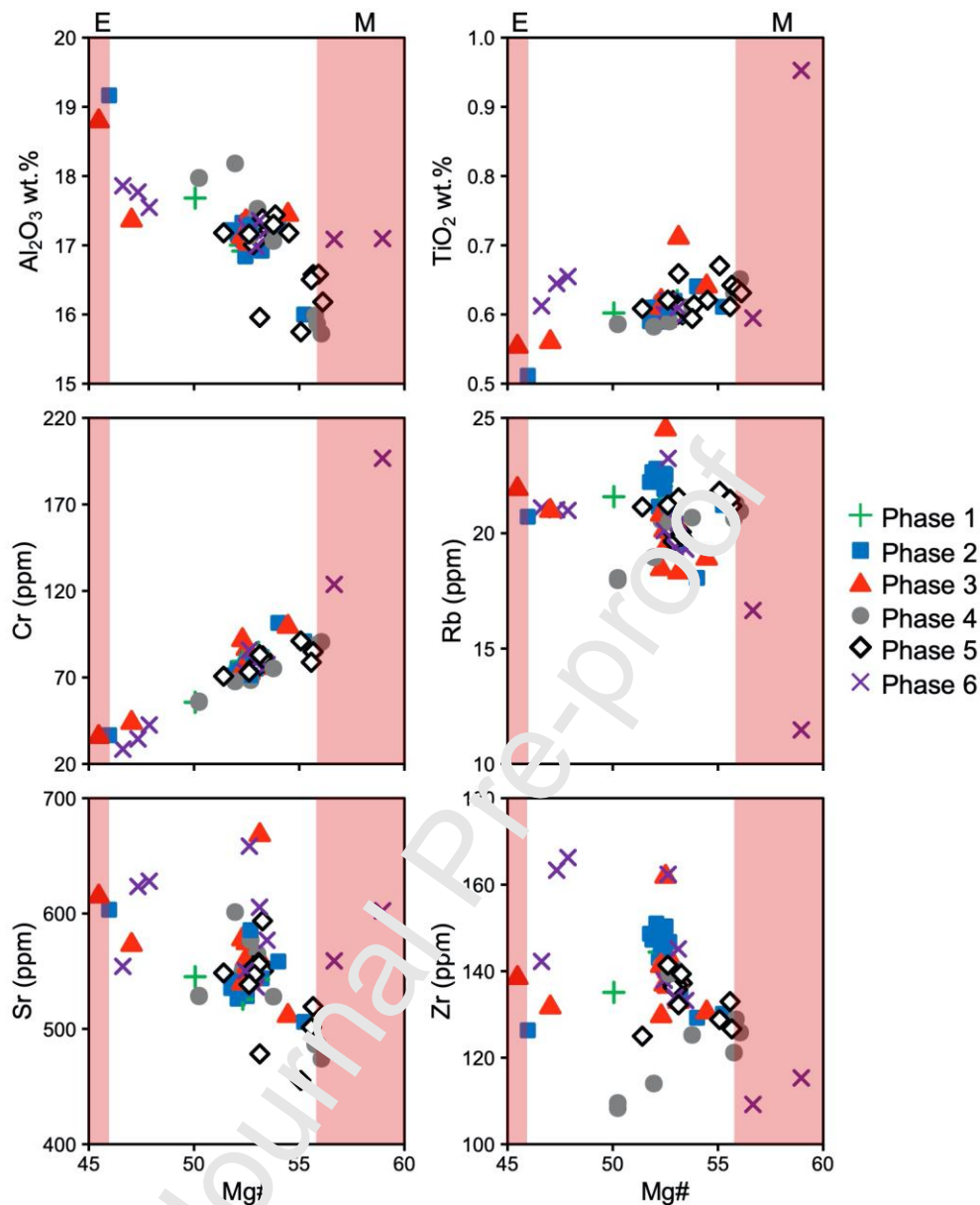


**Figure 4.** Selected major and trace element plots of whole-rock compositions for Volcán de Colima andesites erupted the 2013-17 eruption, plotted against an index of differentiation (Mg-number). Symbolry as in Figure 3. Red shaded areas indicate liquid Mg# ranges which would crystallise equilibrium pyroxenes in the mafic (M) and evolved (E) end members. Equilibrium Mg# ranges for E extend to the left of the axis extents in these plots, and ranges for M extend off to the right of the axis extents.

*[One and a half-page width, 1.5-column, full colour]*

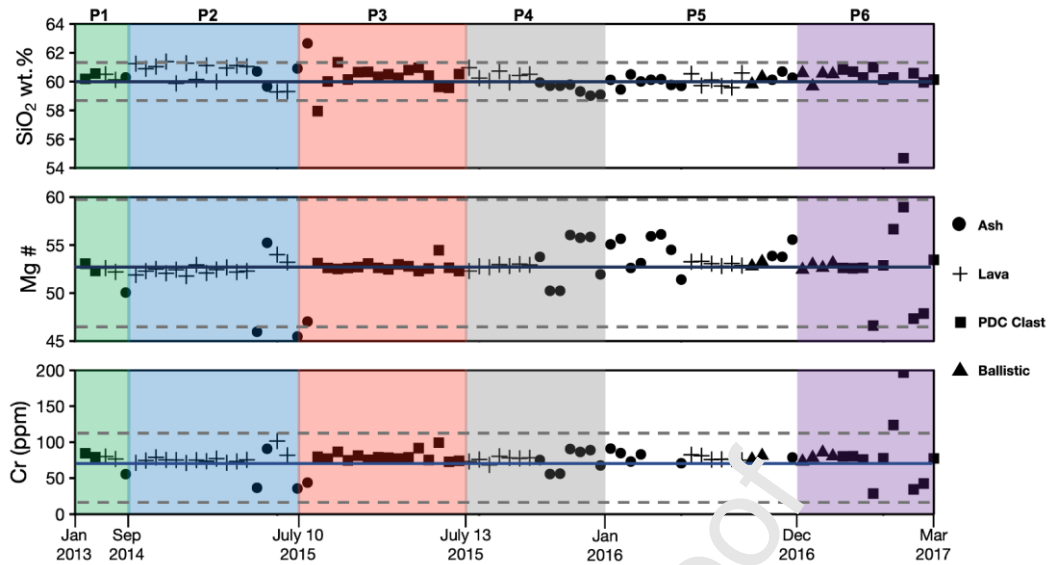


**Figure 5.** Time series of selected sample compositions showing SiO<sub>2</sub>, Mg# and Cr versus time. With the exception of minor deviations (see Section 5.1), most of the time series shows a relatively homogeneous bulk composition of these magmas. Analytical error for all three plots is smaller than the individual points. Blue solid (average) and grey dashed (minima and maxima) lines represent the range of compositions from the post-1915 (1961 to 2005) samples erupted at Volcan de Colima, using data obtained from the GeoROC database (Luhr, 1992, 1997, 2002; Luhr and Carmichael, 1980, 1990; Luhr and Prestegard, 1988; Luhr et al., 2010; Moorbath et al., 1978; Mora et al., 2002; Reubi and Blundy, 2008; Reubi et al., 2017; Robin et al, 1987, 1991; Saucedo et al., 2010; Savov et al., 2008; Verma and Luhr, 2010).

*[One and a half-page width, 1.5 column, full colour]*



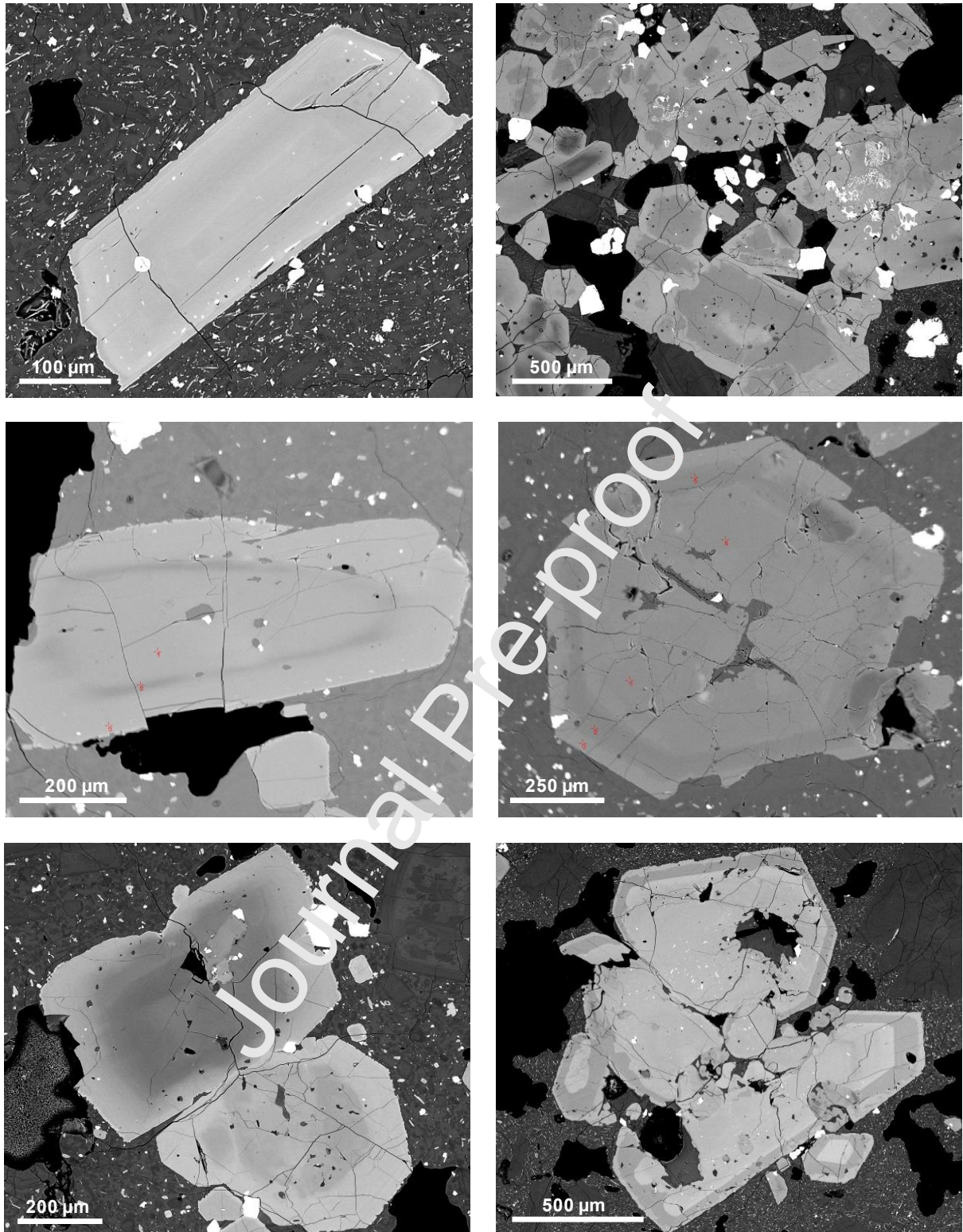









Figure 6 (Caption Overleaf)

**Figure 6.** Pyroxene phenocryst types described in Volcán de Colima samples from the 2013-17 eruption. **A)** Typical low-Mg# homogeneous microphenocryst, with small apatite inclusions near the rim. **B)** Typical pyroxene assemblage within a glomerocryst. The agglomeration contains Normal Zoned, mostly Type 3 crystals, along with remnant olivine, plagioclase, oxides and interstitial melt. **C)** Typical Normal Zoned Type 1 phenocryst with rounded, low-Mg# core mantled by high-Mg# band and low-Mg# rim. **D)** Normal Zoned Type 2 crystal with a rounded core of intermediate composition mantled by high-Mg# band and low-Mg# rim. The reverse-zoned crystals have a similar categorisation, but with the presence of a high-Mg# rim. **E)** Normal Zoned Type 3 crystal with a high-Mg# core rimmed by a low-Mg# rim. **F)** Type 1 Reverse-Zoned crystal with a low-Mg# core rimmed by high-Mg# rim, with sharp core-rim boundary.

*[Full page width, 2-column, B&W]*

Table 1. Summary of pyroxene crystal groups.

Illustration	Description	Zoning (Numbers: Mg#)	Abundance
	<b>Homogeneous</b> Inclusion-rich, low-Mg-number crystal with low magnitude changes in Mg-number across crystal. Common as phenocrysts, in glomerocrysts and as microphenocrysts.	Core, Band and Rim 69-75. Changes of $\leq 5$ across crystal.	Average: 71% (range 62-86) of total phenocrysts, 96% of microphenocrysts, and in 40-65% of glomerocryst pyroxenes.
	<b>Normal Zoned – Type 1</b> Rounded, sometimes embayed, low-Mg core with inclusions mantled by high-Mg band and low-Mg rim.	Evolved Core: 69-75 High-Mg Band: 75-88 Evolved Rim: 69-75	Average: 5% (range 1-10) of total phenocrysts. Very rare (<1%) as microphenocrysts.
	<b>Normal Zoned – Type 2</b> Rounded, core with rare melt inclusions mantled by high-Mg band and low-Mg rim. Core has an intermediate composition between band and rim.	Intermediate Core: 74-84 High-Mg Band: 76-88 Evolved Rim: 69-75	Average: 2% (range 0-3) of total phenocrysts. Absent as microphenocrysts.
	<b>Normal Zoned – Type 3</b> Rounded, high-Mg core with rare melt inclusions. Band occasionally present at intermediate compositions. Rimmed by a low-Mg rim with occasional inclusions.	High-Mg-number Core: 77-89 Intermediate Rim: 77-83 Low-Mg-number Rim: 69-76	Average: 17% (range 7-25) of total phenocrysts. Most abundant zoned microphenocrysts (3%). Most abundant zoned glomerocryst phase (-57%)
	<b>Reverse Zoned – Type 1</b> Inclusion-rich, occasionally rounded low Mg core rimmed by high-Mg rim, with sharp core-rim boundary. Core similar to the ‘Homogeneous’ crystal type.	Core Mg-number 69-76 Rim: Mg-number 77-87	Average: 4% (range 0-10) of total phenocrysts. Most abundant RZ type. Very rare (<1%) as microphenocrysts. Most abundant post-2015 (up to 10%).
	<b>Reverse Zoned – Type 2</b> Rounded, intermediate core with rare melt inclusions mantled by inner high-Mg band and outer low-Mg band. Rimmed by high-Mg rim, with sharp core-rim boundary.	Intermediate Core: 74-84 High-Mg-number Band: 76-88 Low-Mg-number Band: 69-75 High-Mg-number Rim: 78-84	Average: <1% of total phenocrysts. Rarest crystal type. Absent as microphenocrysts.
	<b>Reverse Zoned – Type 3</b> Rounded, high-Mg core with rare melt inclusions mantled by low-Mg band. Rimmed by high-Mg rim, with sharp core-rim boundary.	High-Mg Core: 77-86 Low-Mg Band: 69-76 High-Mg Rim: 77-83	Average: 1% (range 0-2) of total phenocrysts. Absent as microphenocrysts.

[Full page width, 2-column, B&amp;W]

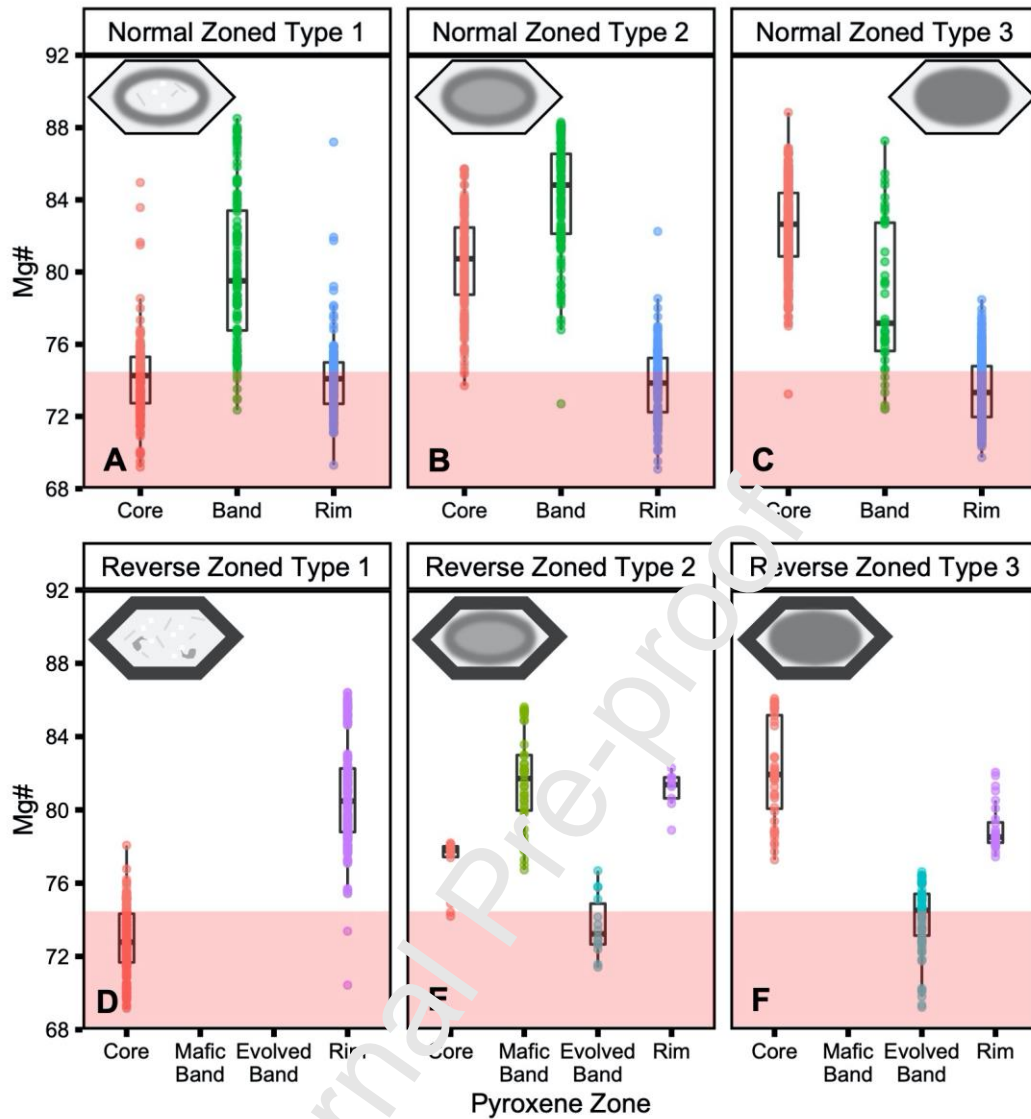


**Figure 7.** Mg# distributions for the major normal and reverse zoned pyroxene phenocryst types, split according to subtype. Box plots show the average (black horizontal bar) and 1 standard deviation distributions at the top and bottom of the box. Pink field shows the typical range of Mg# for Homogeneous-type crystals.

*[One and a half-page width, 1.5-column, full colour]*

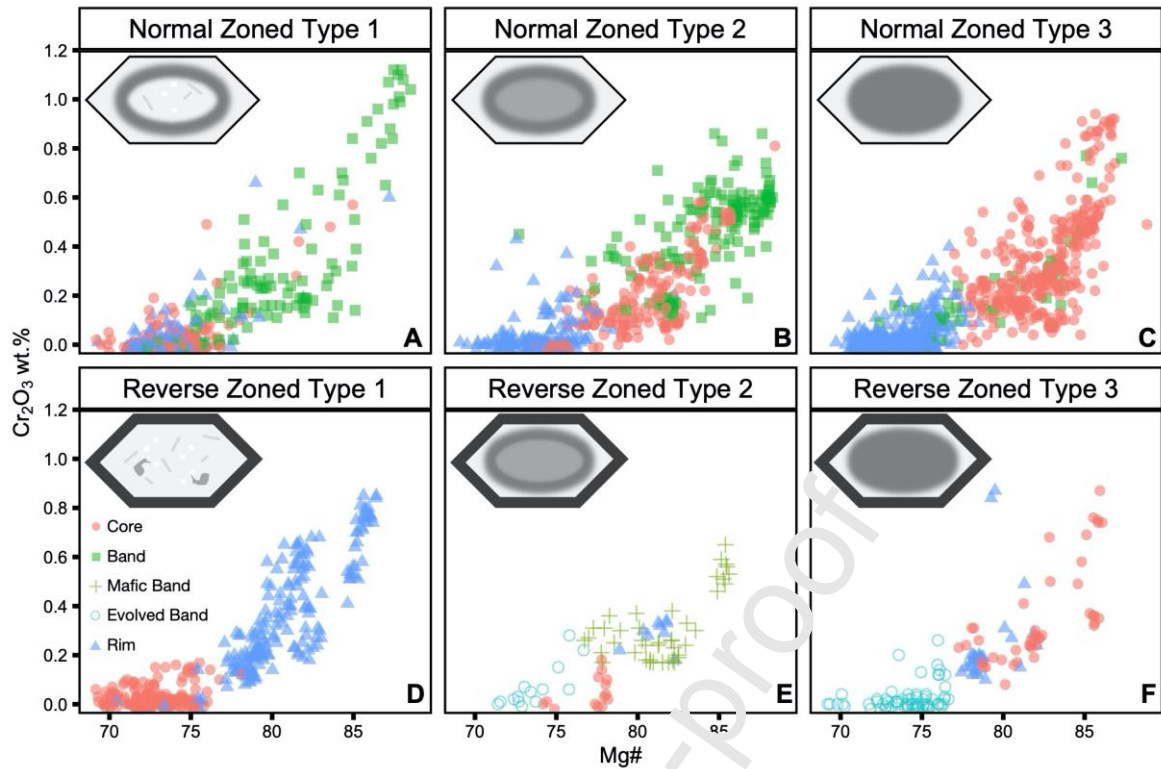


**Figure 8.**  $\text{Cr}_2\text{O}_3$  versus Mg# plots for the major normal and reverse zoned pyroxene phenocryst types, split according to subtype. Normal zoned subtypes have a characteristic high-Mg or intermediate-Mg band marked simply as 'Band' for these plots. Due to the presence of evolved and a mafic bands for the reverse-zoned types, these are differentiated using different symbols. In most cases, higher zone Mg-number is also associated with higher chromium content.

[Full page width, 2-column, full cc'00-1]

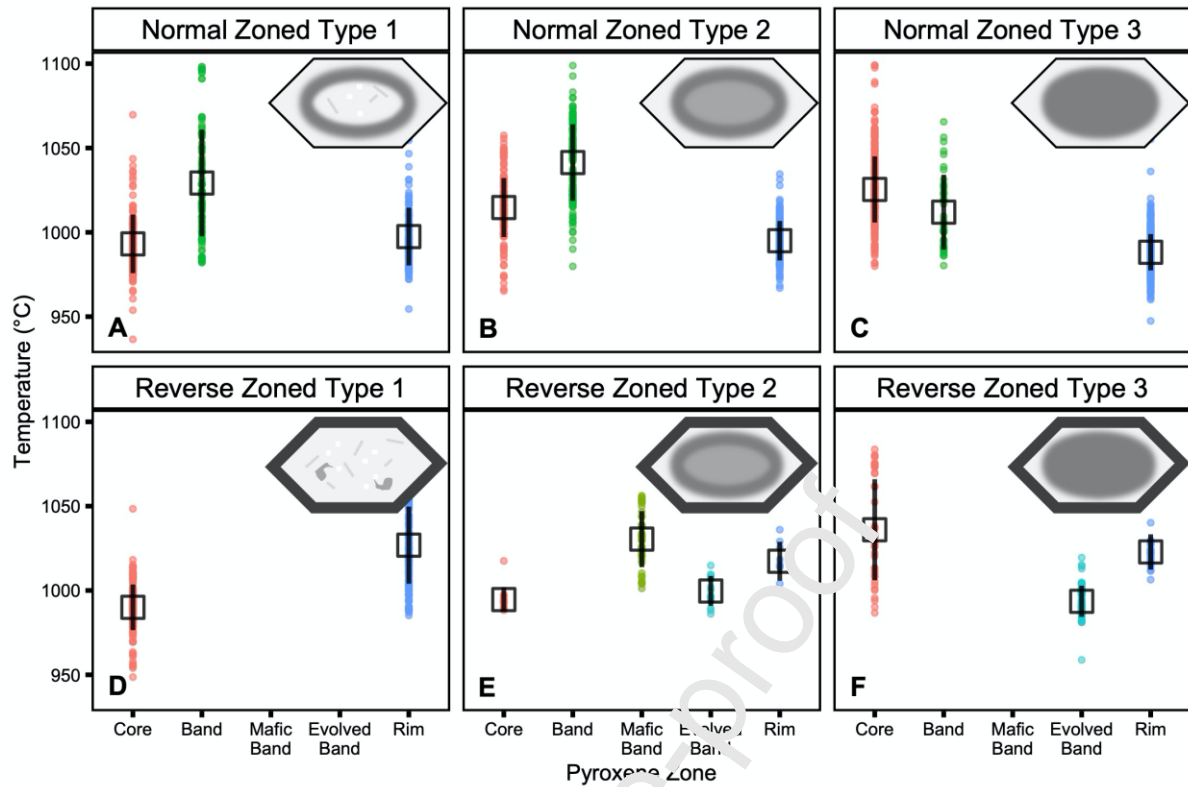


**Figure 9.** Modelled temperature estimates using the two-pyroxene geothermobarometer of Putirka (2008), grouped by crystal zone. Box represents the mean of temperature estimate values and bar represents 1 standard deviation. Colours as per the legend in Fig. 8.

*[Full-page width, 2-column, full colour]*

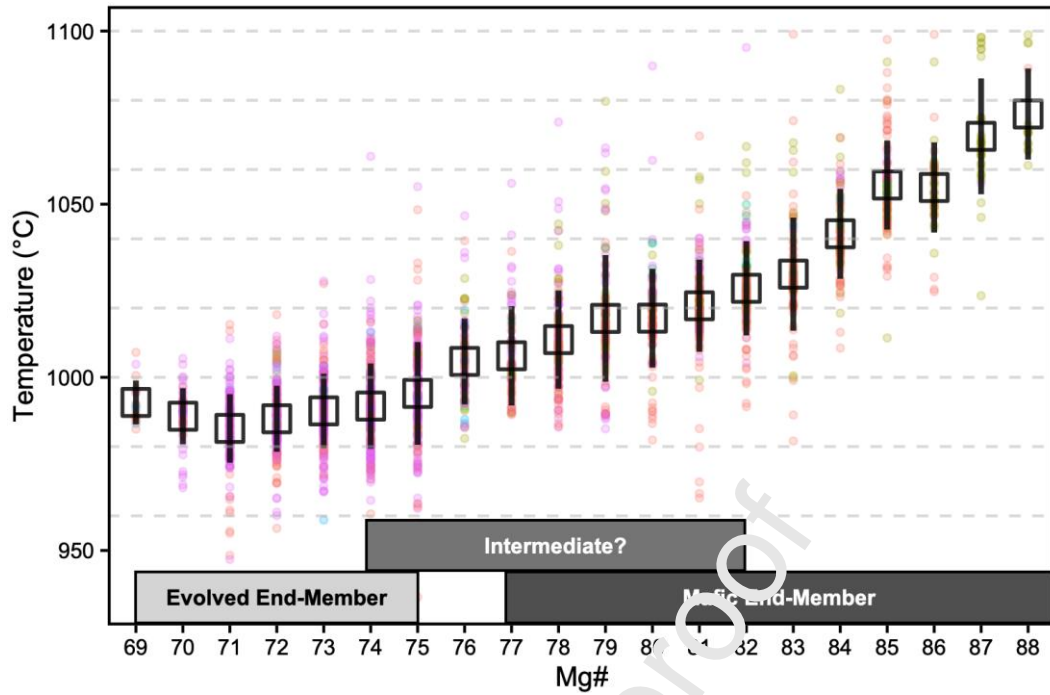


**Figure 10.** Modelled temperature estimates using the two-pyroxene geothermobarometer of Putirka (2008), grouped by Mg#. Box represents the mean of temperature estimate values and bar represents 1 standard deviation. Point colours as per the legend in Fig. 8.

*[One and a half-page width, 1.5-column, full colour]*

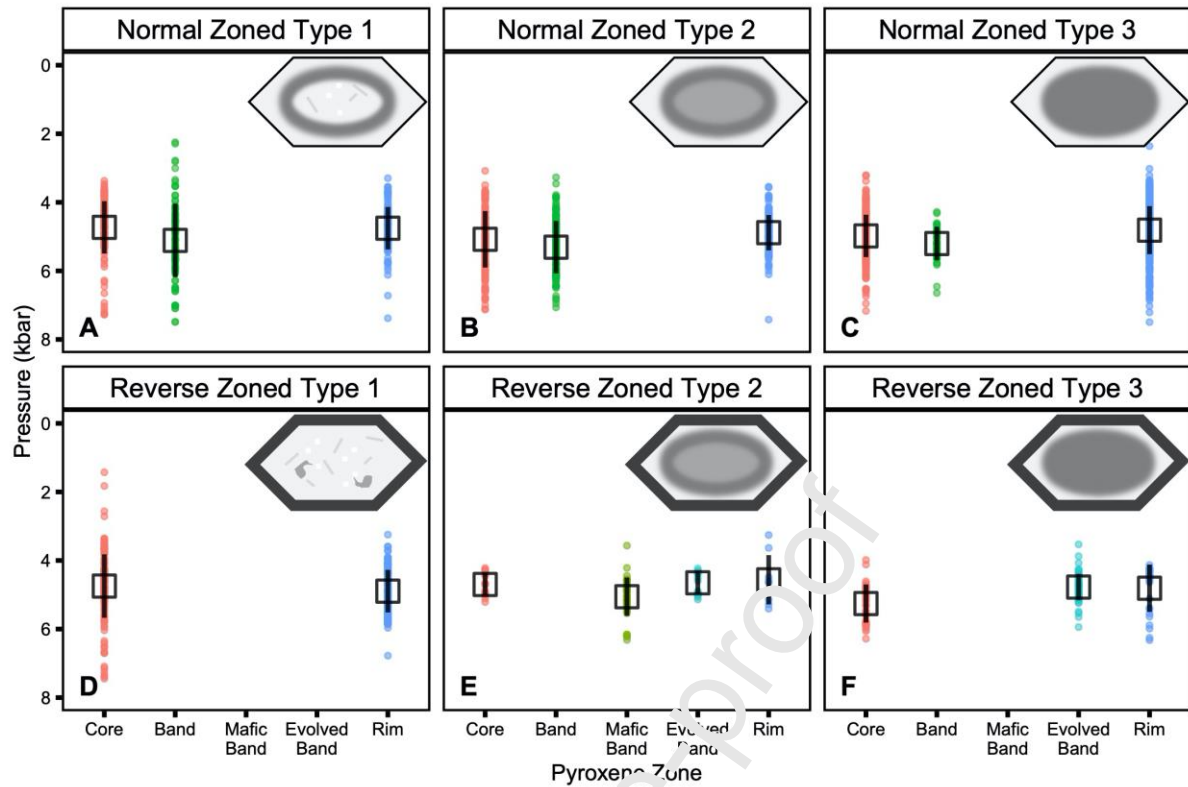


**Figure 11.** Modelled pressure estimates using the two-pyroxene geothermobarometer of Putirka (2008), grouped by crystal zone. Box represents the mean of pressure estimate values and bar represents 1 standard deviation. Colours as per the legend in Fig. 8.

*[Full-page width, 2-column, full colour]*



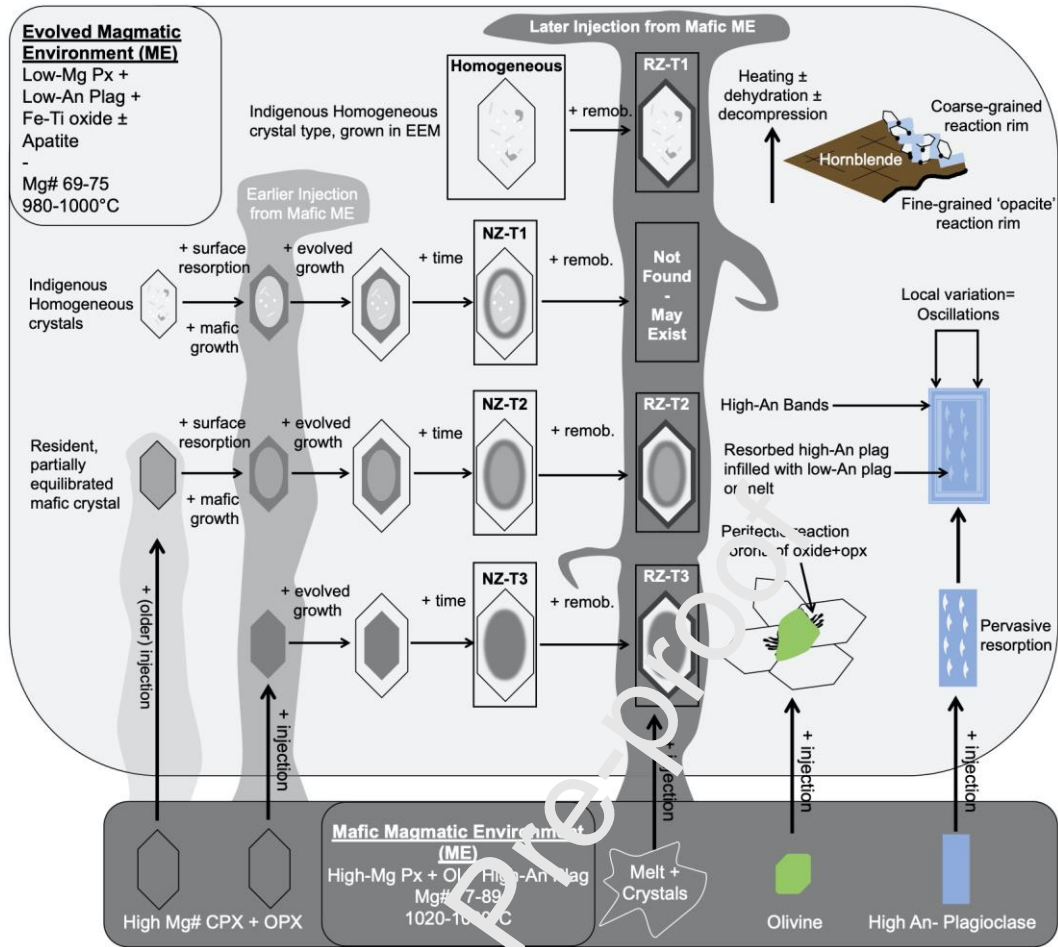


**Figure 12.** Schematic model of the interactions between resident evolved melts and injections of mafic melts from depth in the plumbing system of Volcán de Colima.

[One and a half-page width, 1.5-column, full colour]

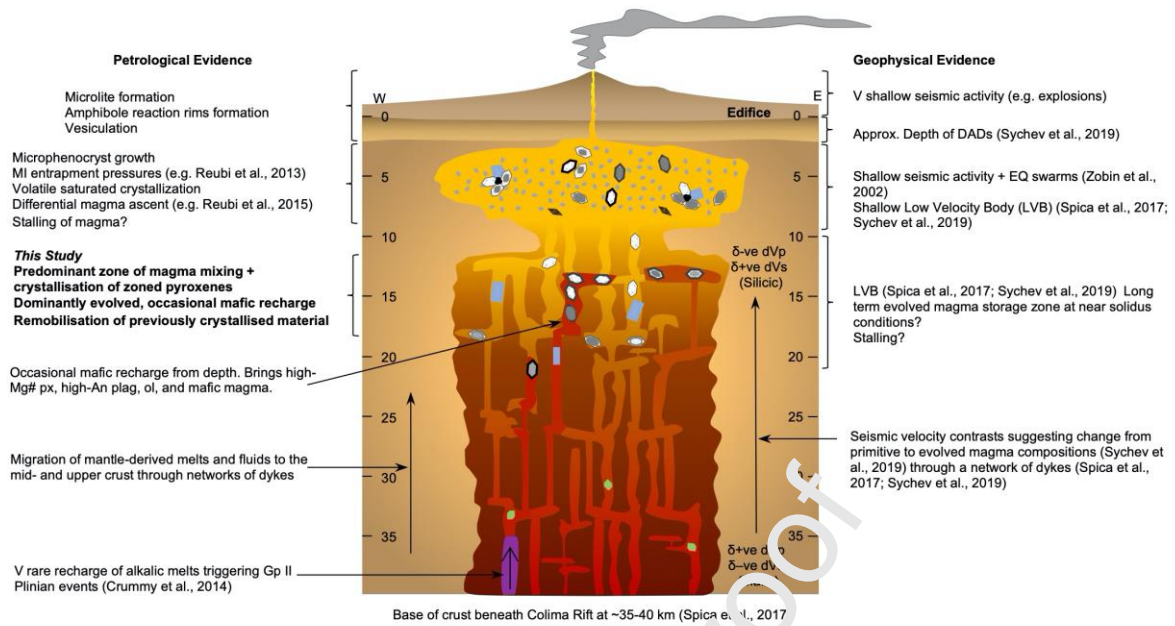


**Figure 13.** Petrological model of the plumbing system of Volcán de Colima, combining petrological information from the findings of this study and published literature, along with geophysical evidence. General abbreviations include px (pyroxene), plag (plagioclase), ol (olivine), EQ (earthquake), DADs (Debris Avalanche Deposits). ‘Gp II’ refer to Plinian events with an alkalic component as described by Crummy et al. (2014).  $\delta$ -ve dVp refer to relative negative dVp values, and  $\delta$ +ve dVs refer to relative positive dVs values, and used as evidence for silicic magmas in this part of the crust by Sychev et al. (2019). References as in the text.

[Full-page width, 2-column, full colour]